

Polarimetric SAR  
Interferometry for Forest  
Aboveground Biomass  
Estimation

Shreya Chandola  
March 2014

**ITC SUPERVISOR**  
Dr. Valentyn Tolpekin

**IIRS SUPERVISOR**  
Mr. Shashi Kumar



# Polarimetric SAR Interferometry for Forest Aboveground Biomass Estimation

Shreya Chandola

Enschede, The Netherlands [March, 2014]

Thesis submitted to the Faculty of Geo-information Science and Earth Observation (ITC) of the University of Twente in partial fulfilment of the requirements for the degree of Master of Science in Geo-information Science and Earth Observation.

Specialization: Geoinformatics

## THESIS ASSESSMENT BOARD:

Chair	: Prof. Dr. Ir. A. Stein
ITC Professor	: Prof. Dr. Ir. A. Stein
External Examiner	: Mr. Sanjay (DEAL, Dehradun)
IIRS Supervisor	: Mr. Shashi Kumar, IIRS
ITC Supervisor	: Dr. V.A. Tolpekin, ITC

## OBSERVERS:

IIRS Observer	: Dr. SK Srivasatav
ITC Observer	: Dr. N.A.S. Hamm

## **DISCLAIMER**

This document describes work undertaken as part of a programme of study at the Faculty of Geo-information Science and Earth Observation (ITC), University of Twente, The Netherlands. All views and opinions expressed therein remain the sole responsibility of the author, and do not necessarily represent those of the institute.

*Dedicated to my Nana Nani....*



## ABSTRACT

---

The regulation of the carbon cycle is a critical ecosystem service provided by forests globally. It is therefore necessary to have robust techniques for speedy assessment of forest biophysical parameters at landscape level. It is arduous and time taking to monitor the status of vast forest landscapes using traditional field methods. Remote sensing and GIS techniques are efficient tools that can monitor the health of forests regularly. Biomass estimation is a key parameter in the assessment of forest health. The estimation of biomass is also crucial to understanding the amount of carbon present globally and the changes that are taking place in the carbon cycle. The advantage of SAR remote sensing in assessing biophysical forest parameters is its ability to penetrate the canopy and cloud cover. The current research work focuses on the retrieval of forest biophysical parameters of the Barkot Forest area, using fully polarimetric C-band data with Polarimetric SAR Interferometry (PolInSAR) techniques. The Interferometric Water Cloud Model (IWCM) has been used to estimate aboveground biomass (AGB). Input parameters to the IWCM have been extracted from the decomposition modeling of SAR data as well as PolInSAR coherence estimation. Coherence amplitude has also been used for tree height estimation. Previous research has studied the overestimation in volume scattering caused by polarization orientation angle shift and how deorientation has helped to compensate for it. Polarization orientation angle shift has been compensated for in this research work. The accuracy assessment for modeled height and AGB has been carried out using field data. The field measured height ranges from 14.3 m to 33 m. The SV ranges from 17.5 to 51.57 ( $\text{m}^3 \text{ha}^{-1}$ ) and the field measured AGB ranges from 112.58 to 356.06 ( $\text{t ha}^{-1}$ ). The modeled vegetation height values range from 15.95 to 26.93 m and the modelled AGB values range from 158.08 to 515.47 ( $\text{t ha}^{-1}$ ). The  $R^2$  value of 0.5, a RMSE of 62.73 ( $\text{t ha}^{-1}$ ) and a percent accuracy of 51% were obtained for the modeled biomass. The modeled field height has a  $R^2$  value of 0.64, a RMSE of 6.2 m and a percent accuracy of 71.5%. The results suggest that it is possible to obtain forest biophysical parameters using a PolInSAR coherence based semi-empirical modeling approach.

**Keywords:** Interferometric Water Cloud Model, Polarimetric SAR Interferometry, coherence, backscatter, biomass, tree height.



## ACKNOWLEDGEMENTS

---

My thanks are due to IIRS, India and ITC, The Netherlands for providing the opportunity to undertake the present task.

I am especially thankful to my IIRS supervisor, Mr. Shashi Kumar, for his patient guidance without which the completion of this work would not have been possible. He helped me overcome my fear of mathematics.

Special thanks are due to Dr. V.A. Tolpekin, my ITC supervisor, for his repeated corrections to my drafts and for encouraging me to use scientific language in this maiden effort.

I also take this opportunity to express my gratitude towards Mr. P.L.N Raju and Dr. S.P.S Kushwaha for having faith in me and for supporting me.

I would like to thank Dr. SK Srivasatav, for his constant encouragement.

I am also grateful to Dr. Y.V.N Krishnamurthy, Director IIRS, for allowing me the opportunity to be part of the Masters program.

I would especially like to thank Unmesh for his time, for making the toughest problems sound so easy and for his constant help and motivation. A big thanks to Deepak for his weekends, for hours of reassurance and for being such an amazing friend. I would also like to thank my friends at IIRS who welcomed me and always gave me reason to smile.

I am also grateful to Chetan Katoch for his unending encouragement, for putting up with all the drama and for the constant encouragement, which carried me through the toughest days.

I owe my heartfelt gratitude to my parents, my sister and my grandparents for their support and affection. They have been my strength and inspiration and their love always motivates me.



# TABLE OF CONTENTS

---

<b>List of Figures .....</b>	<b>iv</b>
<b>List of Tables.....</b>	<b>v</b>
<b>1. Introduction .....</b>	<b>1</b>
1.1. Problem Statement .....	3
1.2. Research Identification .....	4
1.2.1. Research Objective.....	4
1.2.2. Sub-Objectives .....	4
1.2.3. Research Questions .....	4
1.3. Innovation aimed at .....	4
<b>2. Literature Review.....</b>	<b>5</b>
2.1. Biomass .....	5
2.2. SAR Polarimetry (PolSAR) .....	6
2.3. SAR Interferometry (InSAR).....	9
2.4. Polarimetric SAR Interferometry (PolInSAR).....	10
<b>3. Study Area .....</b>	<b>13</b>
3.1. Background.....	14
3.2. Importance of Area .....	14
3.3. Climate.....	14
3.4. Soils .....	14
3.5. Flora .....	15
3.6. Fauna.....	15
<b>4. Materials and Methods .....</b>	<b>17</b>
4.1. Materials .....	17
4.1.1. Satellite Data.....	17
4.1.2. Field Data.....	17
4.1.3. Ancillary Data.....	18
4.2. Methods.....	19
4.2.1. Fieldwork and calculations.....	19
4.2.2. Basal Area.....	20
4.2.3. Stem Volume.....	20
4.2.4. Aboveground Biomass Estimation (AGB) .....	20
4.3. Methodology.....	21
4.4. PolInSAR based parameter retrieval and AGB estimation .....	21
4.4.1. Polarimetric Decomposition.....	21
4.4.2. POLInSAR Satellite data processing.....	24
<b>5. Coherence based, semi-empirical model.....</b>	<b>30</b>
5.1. Model based parameter retrieval .....	30
5.1.1. Transmissivity.....	30
5.1.2. Two-way attenuation.....	31
5.1.3. Vertical Wave Number .....	31
5.1.4. Semi-empirically Defined Coefficient .....	31
5.1.5. Modeled Tree Height Estimation .....	32

5.2.	Water Cloud Model (WCM) .....	32
5.3.	Interferometric Water Cloud Model (IWCM) .....	34
5.4.	Performance Analysis of Modeled Parameters .....	36
5.4.1.	Root Mean Square Error (RMSE) .....	36
5.4.2.	Coefficient of Determination .....	36
5.4.3.	Percent Accuracy .....	36
<b>6.</b>	<b>Results.....</b>	<b>38</b>
6.1.	Fieldwork Results .....	38
6.2.	Polarization Orientation Angle Shift.....	38
6.3.	Parameter Estimation .....	42
6.3.1.	Forest Backscatter .....	42
6.3.2.	PolInSAR Coherence Estimation.....	44
6.3.3.	PolInSAR Coherence Estimation for Height.....	44
6.3.4.	AGB Estimation from IWCM .....	46
<b>7.</b>	<b>Discussion.....</b>	<b>48</b>
7.1.	Polarization Orientation Angle Shift.....	48
7.2.	Backscatter vs. Biomass .....	48
7.3.	Coherence vs. Biomass .....	48
7.4.	Vegetation Height.....	49
7.5.	AGB Estimation .....	49
7.6.	SWOT table .....	50
<b>8.</b>	<b>Conclusion and Recommendations .....</b>	<b>52</b>
8.1.	Conclusion .....	52
8.2.	Recommendations .....	53
	<b>References.....</b>	<b>54</b>
	<b>Appendix 1: Volumetric Equations: FSI .....</b>	<b>58</b>

## LIST OF FIGURES

---

Figure 3-1: Barkot Forest Area.....	13
Figure 4-1: LULC Map of Barkot Forest Area.....	19
Figure 4-2: Sample plot .....	20
Figure 4-3: Methodology .....	21
Figure 4-5: PolInSAR Geometry .....	25
Figure 4-6: Interferogram of HV+VH .....	26
Figure 4-7: Coherence Image .....	29
Figure 6-1: Volume scattering vs. field-calculated biomass for Master image, before deorientation. ....	39
Figure 6-2: Volume scattering vs. field-calculated biomass for Master image, after deorientation. ....	39
Figure 6-3: Difference in values of volume backscattering before and after deorientation .....	40
Figure 6-4: Volume scattering vs. biomass for Slave image before deorientation.....	40
Figure 6-5: Volume scattering vs. biomass for Slave image after deorientation. ....	41
Figure 6-6: Difference in volume scattering values before and after deorientation. ....	41
Figure 6-8: Total forest backscatter vs. biomass for the Master image.....	43
Figure 6-9: Total forest backscatter vs. biomass for the Slave image.....	43
Figure 6-10: Total coherence vs. field biomass.....	44
Figure 6-11: Modeled height vs. Field height. ....	44
Figure 6-13: Field measured biomass vs. Modeled Biomass. ....	46



## **LIST OF TABLES**

---

Table 4-1: Radarsat-2 Data.....	17
Table -4-2: Baseline Information.....	26
Table 7-1: SWOT table.....	50







## 1. INTRODUCTION

Forests are integral to our environment and are essential to the survival of all life around them as they support and provide for all beings [1]. The importance of these ecosystems and the services they provide is unfortunately disregarded today, as they are used primarily to feed our ever-growing demand for resources. The declining ecosystem services could compromise the future of all living beings. The changing temperatures, which are mostly due to anthropogenic activities and the resultant rise in the concentration of CO<sub>2</sub>, are affecting these ecosystems. UN statistics [2] show that 20% of the annual uptake of CO<sub>2</sub> in the atmosphere is due to the deforestation that is taking place globally. One of the main ecosystem services provided by forests is that they regulate the amount of CO<sub>2</sub> in the atmosphere, helping control the greenhouse effect and the subsequent warming it causes. It is therefore necessary to quantify and map trends in ecosystems in order to conserve them.

The estimation of aboveground biomass is helpful in determining the health status of forests. Forests constitute of vegetation and all plants use sunlight to produce energy through the process of photosynthesis. The matter that is produced as a result of photosynthesis is known as biomass. It is the organic matter and the matter, which is present above the ground, is known as aboveground biomass ( $t a^{-1}$ ). The quality of forests is assessed based on two measurements, one is biomass and the other is stem volume. Biomass estimation helps in the assessment of the carbon present globally. It also assesses the changes that are taking place in the carbon cycle and therefore biomass is crucial to the study of carbon and the carbon cycle.

Remote Sensing and GIS applications have made it relatively easier to monitor the overall health of forests. Various components of forests, like tree heights, diameter and volume of stems, basal area and aboveground biomass can now be easily studied using the advanced remote sensing and GIS technologies. Radar remote sensing is different from visual remote sensing as it uses the microwave (1 mm to 1 m) section of the electromagnetic spectrum to obtain these images of the Earth. Microwave remote sensing is especially useful in areas of high cloud cover as it is able to penetrate through clouds. It is also a vital technique in studying the biophysical characteristics of forests, as the waves are able to penetrate the canopy. Stem volume, tree height and biomass estimation are few of the characteristics that can be easily estimated using microwave remote sensing [4]. The device that emits these wavelengths also records the backscatter that is reflected back after the signal hits the target. Microwaves can penetrate clouds, rain, smoke, forest canopies as well as features below the surface of the Earth. Their ability to penetrate through forest canopies makes microwaves especially useful in the study of biophysical characteristics of forests. The penetrative powers

of microwave remote sensing help in gathering data about the forest canopy, the stems present in the forest and the surface and surface cover of forests [3].

Radar has traditionally been used for target detection but is now increasingly being used for Earth observation. The satellite transmits electromagnetic waves towards an object using an antenna. It then records the received signal that is scattered back from the object. Radar are longer in their wavelength than visible light and are therefore able to penetrate forest canopies which makes them very useful for studying forest bio-physical characteristics. Synthetic Aperture Radar (SAR) uses the Doppler Effect to synthesize a larger antenna, which overcomes the limitations of RAR. SAR Polarimetry (PolSAR), SAR Interferometry (InSAR) and Polarimetric SAR Interferometry (PolInSAR) are techniques that arise from SAR and are vital in the geosciences field today.

SAR Polarimetry is the method in which radar transmits and receives signals in various polarisations. It then records and measures the backscattered signals that vary according to the characteristics of the target [4]. From these measurements a scattering matrix is created. This matrix is useful in understanding the way in which the image pixels respond to the various polarizations arrangements.

SAR Interferometry is the study of analyzing and combining the signals of the same target from differing angles and/or at different times. The combination of the two coherent images is then used to generate a phase difference between the two images. This is also known as an interferogram.

PolInSAR is a solution to several of the limitations that are present in SAR polarimetry and SAR interferometry techniques. It generates interferograms for polarized (transmitted and received) waves. The interferogram phase is dependant on the polarization of the wave and it changes according to the polarization. This phase change in the interferogram is advantageous in the extraction of biophysical characteristics of a medium. PolInSAR has proven to be more effective [4] than PolSAR and INSAR alone. It is an useful mechanism in measurement and prediction of forest characteristics like aboveground biomass (AGB) and height of forests [5].

Estimating forest biomass is vital to the understanding of carbon fluxes and ecological modeling [6]. The traditional optical remote sensing techniques are limited in their estimation of aboveground biomass. SAR technique evaluates the backscatter amplitudes to compute forest biomass. This method has its limitations, though, as it is only able to estimate the biomass for forests that have a biomass less than  $150 \text{ (t a}^{-1}\text{)}$  or below [7]. This is known as the saturation problem. This limitation is addressed by PolInSAR, which, is a coherent combination of SAR interferometry and polarimetry [5]. It is considerably more effective in detecting and measuring forest parameters. This technique is an alternative method that uses forest height to estimate AGB. One of the ways in which AGB is calculated is from forest

height using allometric equations [5]. Forest height and biomass are proportional to each other in terms of growth [8].

Various researches have been carried out on biomass estimation. Neumann[9] focused on Polarimetric SAR Interferometry, its theory and its modelling. He also investigated PolInSAR coherence and its properties. Cloude and Papathanassiou [10] have studied the role of coherence optimization in PolInSAR. Santoro [11] used the Water Cloud Model (WCM) and the Interferometric Water Cloud Model (IWCM) to relate backscatter and coherence to stem volume. He focused on retrieving forest biophysical characteristics using ERS and JERS imagery. Mette [12] studied biomass estimation using PolInSAR techniques. The project used allometric equations to extract forest height from PolInSAR data. Many studies till date have used L and P bands in their research of forests as it these waves have deeper penetration ability and are able to estimate higher biomass values. The current research focuses on the use of SAR backscatter and PolInSAR coherence to estimate aboveground biomass.

### **1.1. Problem Statement**

The decomposition modeling that is carried out using a scattering matrix is useful in studying the various scattering elements that take place within one single SAR pixel [13]. Previous studies have recorded and studied the backscatter from forests using the SAR backscatter technique using single polarization technique. The limitation of this technique, though, is that after a certain volume of biomass the SAR backscatter technique reaches a saturation point after which it is unable to procure more information about the biomass of the forest.

The main setback of polarimetry in vegetated areas is that of high entropy. Entropy is a measure of disorder. The main problem is that in polarimetry the scattering that occurs from the vegetation leads to low coherence values in the polarized channels. This is known as depolarization. This leads to limited use of polarimetry over vegetated areas. PolInSAR is advantageous in this manner because it overcomes this limitation, as the different polarization combinations coupled with interferometry are able to better address the saturation problem in aboveground biomass estimation.

Interferometry also does not work well in highly vegetated areas as interferograms can be generated because of various physical affects which can overshadow any valuable information from the data[14]-[15]. Though interferometry addresses the issue of low coherence through the use of baseline selection it is PolInSAR, which is most useful for forestry applications as it is able to obtain high coherence values for all of the polarized channels. The estimation of forest parameters, especially biomass estimation has greatly benefitted from PolInSAR techniques. The height of objects can also be easily obtained from this technique, which is why it is useful in the estimation of forest height.

Previous studies show that it is difficult to extract backscatter information from single or dual polarized data. Fully polarimetric data allows to extract information on all scattering parameters from a single SAR resolution cell. With the help of fully polarized data one can identify the contribution of ground, ground-stem interaction and canopy to total backscatter. The current project uses fully polarized data with semi-empirical modeling to estimate AGB.

## **1.2. Research Identification**

### **1.2.1. Research Objective**

The current research explores the potential of PolInSAR based coherence in modeling forest aboveground biomass.

### **1.2.2. Sub-Objectives**

1. To generate 6×6 coherency matrix using fully polarimetric SAR images
2. To identify the coherence between HH, VV, VH and HV images
3. To define the IWCM parameters needed for AGB estimation
4. To calculate forest height using PolInSAR coherence estimation
5. To validate the estimated forest aboveground biomass using field data.

### **1.2.3. Research Questions**

The research objectives are framed into a set of research questions.

1. How can PolInSAR based semi-empirical modeling be used to estimate AGB?
2. How can the 6×6 coherency matrix be used to give parameters needed for the IWCM?
3. What is the relationship between coherence and biomass and backscatter and biomass?
4. How can tree height be calculated using PolInSAR coherence estimation?
5. What modeling parameters are required to model forest aboveground biomass using the IWCM?
6. To what degree is the resultant forest AGB estimation using the PolInSAR technique similar to the AGB estimated from the fieldwork?

## **1.3. Innovation aimed at**

The innovation is aimed at modeling forest aboveground biomass using PolInSAR techniques with fully polarimetric data.

## 2. LITERATURE REVIEW

### 2.1. Biomass

Forests are ecosystems that cover almost 30% of the Earth's terrestrial area. They are vital to the survival of all beings as they are a pool of natural resources [6]. Biomass is a crucial parameter in evaluating the health of a forest. It is the sum of the living mass that is present above and below the ground, like trunks, leaves, branches and roots. Collecting information on below ground biomass can prove to be difficult and therefore most studies concentrate on AGB [16]. The biomass of a forest is described in terms of the living organic matter that is present above ground and it is expressed as the mass of the living material that is present per unit area of forest.

There are four ways of estimating biomass, harvest sampling technique, non-destructive sampling, airborne/space borne remote sensing data and estimating biomass through modelling [17].

The harvest sampling technique is also known as destructive sampling. This method divides the vegetation into various components like branches, leaves, stems and twigs. The fresh weight and the oven-dried weight of these components are measured and biomass is estimated.

The non-destructive sampling technique is a simple and economical alternative to the destructive sampling technique as it involves the use of a variety of regression modelling to estimate biomass, which does not require sample collection. This technique is especially useful in those areas that are inaccessible and also in those areas where the vegetation is largely heterogeneous.

Remote sensing data can be obtained in various spatial and temporal resolutions. It has proven to be reliable in collecting data in those areas that are inaccessible otherwise. This data also provides complete spatial coverage [18].

Biomass can also be estimated using various models. Goel [19] reviewed 32 vegetation canopy models that measure and retrieve various forest parameters and estimate biomass. The variables collected from the field are used in allometric equations to estimate biomass. The major challenge with using empirical models is that they do not work in areas with high vegetation diversity. Semi-empirical models overcome this limitation by considering the theoretical as well as the observational values [20].

Optical data is another way of estimating biomass [21]-[22]. The main disadvantage of optical remote sensing is that the wavelengths in the optical range are unable to penetrate cloud cover. Optical remote sensing uses the Sun's radiation to sense objects and therefore does not work at night or in unfavorable weather conditions. Microwave remote sensing overcomes this limitation. Microwaves are longer in length and are able to collect data at night and in cloudy conditions as well [23]-[24]. Also, unlike optical remote sensing, radar is able to sense the geometry of an object. Radar plays an important role in research and has diverse applications today [23]-[25]. Various polarization combinations can be used to gain structural information on any target [17]. Microwave has also been especially useful in studying the biophysical characteristics of forests.

The frequency of a wave determines its subsurface penetration depth; the longer the wavelength the deeper the penetration [26]. Various microwave bands (X, C, L, P etc.) have been used in previous studies to estimate the biophysical characteristics of different vegetation types [5],[27],[28]. P and L bands have lower frequency than X and C bands. The L and P bands tend to scatter more in the trunks and branches of a forest as these waves are able to penetrate deeper. The X and C bands tend to scatter more in the canopy as these have higher frequencies [29]. The scattering of the EM wave depends on object as well as system characteristics. Object characteristics include surface roughness, dielectric constant of the object, the orientation angle and slope angle. The system characteristics are wavelength and frequency of the radar, look angle, look direction and polarization [23],[30].

SeaSAT, the first radar satellite was launched in 1978 with LandSAT. After that several other shuttles like SIR-A/B(1981), SIR-C(1994), JERS-1 (1992), RadarSAT (1995), EnviSAT (2002), TerraSAR X (2007) and RadarSAT -2 (2007) have followed and continuous microwave data has been acquired [12].

## **2.2. SAR Polarimetry (PolSAR)**

Numerous studies have studied the potential of PolSAR and explored how polarimetry can contribute towards solving problems that exist in remote sensing [24],[31],[32]. PolSAR consists of acquiring, producing and analyzing various polarization states of an EM wave. The polarizations allow the measurement of complete target information. Sinclair, [33],[34] studied those system properties that transmit waves in various polarizations with differing orientation angles and ellipticity. He then developed techniques that assess the performance of these systems. Kennaugh [35],[36] presented the theory of optimal polarizations. Kennaugh's idea was further explored by Huynen [37], who also introduced the target scattering matrix decomposition.

Fully polarimetric raw data is provided in Single Look Complex (SLC) format. The spatial resolution of the SAR data is a product of azimuth and range resolution. Azimuth resolution is the along track measurement and range resolution is the across track. The raw data image is presented in slant range and it represents the actual distance of the target from the radar. The objects that fall in the near range are compressed compared to the ones in the far range. The multilooking process averages the pixels and azimuth and range resolutions become equal.

The PolSAR technique can be used to classify various scattering mechanisms in complex systems and is then able to decompose them to identify the basic objects that the scattering occurs from. This ability of PolSAR is useful in the detection, categorization and segmentation of objects [38]. A fully polarimetric system is able to record all polarization combinations. A radar system transmits and receives waves with differing polarizations as the target can change the polarization of the transmitted wave. A system that uses both horizontal (H) and vertical (V) polarizations has four polarization channels which are HH, VV, HV and VH, where HH means that a horizontally polarized wave has been transmitted and received, HV means that a horizontally polarized wave has been transmitted and a vertically polarized wave has been received and so on [26]. The HH and VV are called like-polarized waves whereas HV and VH are called cross-polarized. Three levels of polarizations exist in a radar system. Single polarization consists of either HH or VV or HV or VH. Dual polarization can be a combination of HH and VV or HH and HV or VV and VH. Quad polarization refers to a system that has a combination of all polarizations; HH, VV, HV and VH.

The values measured from these channels are presented in form of a 2×2 matrix known as the scattering matrix. The polarization information that is available in the radar images is dependent on the geometry and the orientation of the object as well as its geophysical characteristics like surface roughness, moisture content, etc. This information can be obtained from a 2×2 matrix [39].

$$S = \begin{bmatrix} S_{HH} & S_{HV} \\ S_{VH} & S_{VV} \end{bmatrix} \quad (2-1)$$

The scattering matrix that is obtained for each pixel of the SAR image constitutes of four elements that are known as the complex scattering amplitudes. Monostatic and bistatic are two types of transmitter-emitter configurations of radar systems. Monostatic systems have one antenna, which transmits and receives waves while bistatic systems transmit and receive waves separately. In monostatic systems, reciprocity is always assumed, which means that  $S_{HV} = S_{VH}$ . Reciprocity reduces the number of independent elements of the scattering matrix from four to three and it makes the scattering matrix symmetrical.

Analysis of the scattering matrix (2-1) is effective only when targets are coherent or pure. Complex targets, like vegetation, can be analyzed using the coherency or covariance matrix [31],[40]. The coherency matrix is a 3×3 matrix [T] and it is able to extract polarimetric parameters for complex targets. Huynen [37] and Lee [41] demonstrate that the coherency matrix [T] can be obtained using linear combinations. This 3×3 coherency matrix results in nine parameters that contain the physical information of the target.

$$\begin{aligned} < |T| > & \hspace{15em} (2-2) \\ = & \left[ \begin{array}{ccc} < |S_{HH} + S_{VV}|^2 > & < (S_{HH} + S_{VV})(S_{HH} - S_{VV})^* > & 2 < (S_{HH} + S_{VV})S_{HV}^* > \\ < (S_{HH} - S_{VV})(S_{HH} + S_{VV})^* > & < |S_{HH} - S_{VV}|^2 > & 2 < (S_{HH} - S_{VV})S_{HV}^* > \\ 2 < S_{HV}(S_{HH} + S_{VV})^* > & 2 < S_{HV}(S_{HH} - S_{VV})^* > & 4 < |S_{HV}|^2 > \end{array} \right] \end{aligned}$$

Decomposition of the coherency matrix results in scattering powers that analyze the surface, double bounce and volume scattering taking place in a distributed target (natural systems like forests). These target generators can be used to create color-coded PolSAR images, which can then be analysed to see how much each scattering component contributes to the total backscatter.

The parameter that is affected by shift in polarization orientation angle is  $T_{23} = (2(S_{HH} - S_{VV})S_{HV}^*)$  [42]. The shift in the orientation angle is induced by irregular terrain and it causes rotation of the backscattered wave [43]. The orientation angle shift is a function of the range and azimuth slopes as well as the radar look angle. The direction of the wave changes when it scatters from the target. The shift in the orientation angle is the difference caused in the angle and the direction of the backscattered wave from the incident wave. The resulting backscatter and the shift in orientation angle also depend on the geometric characteristics of the target [44]. The orientation angle shift is evaluated using the following expression:

$$\tan \theta = \frac{\tan \omega}{-\tan \gamma \cos \varphi + \sin \varphi} \quad (2-3)$$

Where  $\omega$  represents the azimuth slope,  $\gamma$  the ground range slope and  $\varphi$  is the radar look angle.

The polarization orientation angle is a geometrical parameter that describes the ellipse polarization. The following equation is able to derive the orientation angle

$$\theta = \{ \text{Arg}(\langle S_{RR} S_{LL}^* \rangle + \pi) \} / 4 \quad (2-4)$$

Where  $\langle \rangle$  indicates multilooking,  $*$  is the complex conjugate,  $\text{Arg}(\langle S_{RR} S_{LL}^* \rangle)$  is the phase and  $\pi$  is added in order to unwrap the phase. The subscripts RR (right transmit receive) and LL (left transmit receive) signify the polarization combination in a circular polarized wave. Unwrapping the phase extracts information on the surface of the slope and its alignment.

De-orientation focuses on rotating the coherency matrix to a specific orientation where cross polarization is minimized [45] and It reduces the randomness present in the orientation of the scatterers [46]. The de-orientation illustrates the shift in the orientation angle from the target orientation. The effects of orientation angle shift on a  $3 \times 3$  coherency matrix and its decomposition were studied by Lee and Ainsworth [47]. They found that orientation angle shift leads to an increase in the amount of volume scattering. Further, they found that the orientation angle compensation reduced the amount of contribution to total backscatter from volume scattering and resulted in an increase of the double bounce scattering whereas a slight difference in the surface scattering was noticed.

The objective of the various decomposition models is to express the total backscatter as a sum of various scattering mechanisms (volume scattering, double bounce and surface scattering). There are two types of decompositions: coherent and incoherent [48]. Coherent decompositions are those that describe the scattering that occurs from coherent or pure targets. This type of decomposition can be described completely by the scattering matrix alone.

Incoherent decomposition uses the coherency matrix to describe the scattering behaviour of a natural medium like forest. The Freeman and Durden [13] model considers three scattering mechanisms; volume scattering, double bounce and surface scattering. The volume scattering results from randomly oriented dipoles, double bounce is a result of the wave hitting orthogonal surfaces and the surface scattering is a resultant of the wave hitting a surface and being reflected back. The Yamaguchi [49] model adds another scattering mechanism to the three-component model. This new component is the helix scattering and adding the fourth component results in a clearer distinction of vegetation areas from urban areas. A model for urban areas was suggested by Moriyama [50]. Zhang et.al. [51] extended the four-component model and developed the Multiple Component Scattering Model (MCSM).

### **2.3. SAR Interferometry (InSAR)**

SAR interferometry utilizes the information gained from the phase difference of two SAR images. The phase difference image that is generated can also be called an interferogram [52].

The images can be acquired using single-pass or repeat-pass interferometry. Single-pass interferometry consists of mages that are taken on the same day and spatial decorrelation must be taken into account. Spatial decorrelation is the decorrelation that occurs due to changes in the spatial positions of the satellite where the images are taken from. Repeat-pass

interferometry is when images are taken with a time difference and both spatial and temporal decorrelation are measured [12]. Caro et al. [53] were the first to utilize single pass interferometry. Zebker and Goldstein [52] were the first to produce interferograms. Li and Goldstein [54] produced interferograms that were generated using repeat pass interferometry for the first time.

The interferogram is a product of the pixels of image 1 (master image) and the conjugate of the pixels of image 2 (slave image). The two images must be co-registered before the interferogram is generated. The interferometric coherence is also used to extract target information. InSAR extracts 3D information of the target and is also useful in generating digital elevation models (DEM). InSAR uses images taken from two slightly different points, which results in a baseline between the sensor, which is the distance between the two sensors. It uses volume decorrelation in extracting the height of volume scatterers. Mette [12] has used this technique to extract forest height.

InSAR has many applications in forestry. It used to differentiate various forest types [55],[56] and is useful in the estimation of height and biomass. It is especially useful in forestry because it is sensitive to forest structure. Santoro et al. [57] estimated biomass using coherence-biomass techniques while Papathanassiou and Cloude [58],[59] estimated height using PolInSAR height inversion.

#### **2.4. Polarimetric SAR Interferometry (PolInSAR)**

PolInSAR images combine two polarimetric images using interferometry. Cloude [4] describes this technique as the combination of two polarimetric coherency and covariance matrices, which define the polarimetric and interferometric correlation that exists between the two images. Cloude and Papathanassiou [10] were the first to introduce PolInSAR. This technique was further developed when the RVoG model was introduced by Treuhaft and Siqueira, Cloude and Papathanassiou, Papathanassiou and Cloude [15],[58],[60]. Several studies, today, have used PolInSAR to retrieve structural information on forests [5],[61], agricultural lands [62],[63] and urban areas [64],[65]. Many studies have also been carried out on the optimization of PolInSAR coherence [58],[66],[67]. Mette et.al. [5] used PolInSAR to estimate biomass of boreal forests. Imhoff [9] used multibase line PolInSAR for vegetation modeling and forest parameter retrieval.

When observing a natural medium from two different positions, two scattering matrices are produced. The vectorized form of the scattering matrix is used to develop coherency and covariance matrices. Two such  $3 \times 3$  coherency [T3] matrices are used to generate a  $6 \times 6$  complex coherency [T6] matrix [4]. A [T3] matrix uses the polarizations to define characteristics of the object and a [T6] matrix is the interferometric combination of two [T3] matrices. The polarimetric component can be seen in the scattering mechanism and the

interferometry comes from repeated observation of the target from two different look angles. Coherence between two images is basically the complex correlation coefficient that exists between them. Degree of coherence between the two images explains the interaction of polarimetry and interferometry in PolInSAR [68].

Coherence ( $\gamma$ ) is a correlation between two SAR images and depends on the characteristics of the target being observed in addition to the features of the radar system. Zebker and Villasenor [69] outlined three correlation sources that measure coherence. Forestry applications focus on three decorrelation sources, which are, temporal ( $\gamma_t$ ), spatial ( $\gamma_s$ ) and system noise correlation ( $\gamma_{snr}$ ). The spatial and temporal correlations are a result of decorrelations that take place due to the scatterer. The system noise correlation results from processing and system related properties. If these correlations are known for all polarizations then the degree of coherence can be measured [68]. The PolInSAR technique separates the various sources of correlation that go into calculating the total degree of coherence ( $\gamma$ ).

This chapter has reviewed the research that has studied the estimation of biomass and other forest parameters using PolSAR, InSAR and PolInSAR. It has been seen that PolInSAR is an effective technique for estimating forest biophysical characteristics. Previous studies have mainly focused on estimation of biomass through coherence optimization and the estimation of forest height through PolInSAR inversion. The current research focuses on PolInSAR based optimized coherence for the modeling of AGB.



### 3. STUDY AREA

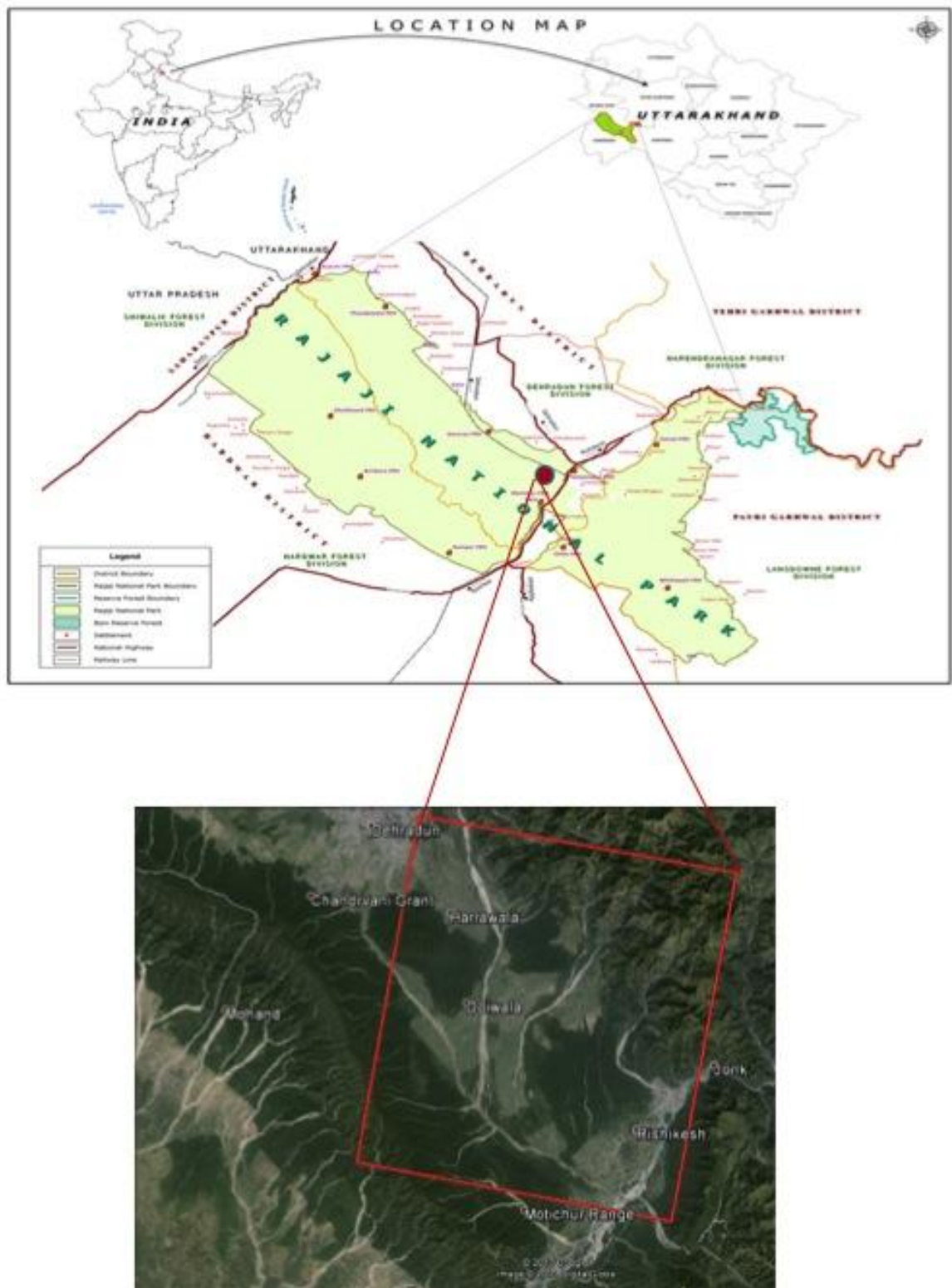


Figure 3-1: Barkot Forest Area

### 3.1. Background

The study area for this project is the Barkot Forest area, which is found in the state of Uttarakhand situated in Northern India. The location being studied has an area of 1800 km<sup>2</sup>. The Ganges River passes through this region making it ideal for agriculture. The region is famous for large-scale production of agricultural crops. The patch of forest area that is studied borders the Rajaji National Park, which is famous for its flora and fauna. The northern portion of the Barkot Forest area is covered by dense Sal (*Shorea robusta*), and Kair-sissoo (*Acacia catechu*, *Dalbergia roxburghii*) forests. The southern part of the forest is a diverse mixture of various grasses, shrubs and bamboo.

### 3.2. Importance of Area

The Sal forest that is found in this area is interesting to study as its dense canopy contributes to volume scattering. The surrounding agricultural area, during the growing season, is another contributor to volume scattering. The same agricultural areas, when there are no crops growing on it, contribute to surface scattering. Interactions between the non-vegetated areas and the forests are responsible for double bounce and can also be studied here.

This area provides the opportunity to study all types of backscatter in one area and this fulfills the aim of the project which is to study the various types of scattering (volume, double bounce and surface) that take place in a forest. The terrain is not undulating and therefore there is no need for an external DEM, which is why this area was chosen. Collection of the field data was also easy as it is in close proximity to the institution.

### 3.3. Climate

The climate in this area is moderate to cold as it is located in the foothills of the Himalayas. The area experiences monsoons from June till September and winter rains in December and January making the annual average precipitation about 2073.3 mm. In the summer the temperatures range from 23 to 41<sup>0</sup>C and in the winters it can be anywhere from 5 to 23<sup>0</sup>C.

### 3.4. Soils

Inceptisol, Molisol and Alfisol make up the soil in this area. The soil is coarse and loamy and ranges from acidic to neutral [70].

### 3.5. Flora

Champion and Seth [71] have classified the Dehradun district into three types of Sal forest, which are, Moist Shiwalik Forest, Moist Bhabar Doon Sal Forest and Dry Shiwalik Sal Forest. The Barkot forest area consists mostly of the Moist Shiwalik Sal Forest. The Moist Bhabar and Moist Shiwalik Sal are found in patches in the souther slopes of this area. Sal (*Shorea robusta*), Chamror (*Ehretia laevis Roxb.*), Sagaun (*Tectona grandis L. f.*), Kanju (*Holoptelea integriflora (Roxb.) Planch.*) and Rohini (*Mallotus philippensis (Lamk) Muell.-Arg.*) are the tree species that are mainly found in this forest type. Lantana (*Lantana camara*) is a weed that has greatly affected the rejuvenation of the forest in this area and is especially harmful for Sal.

### 3.6. Fauna

The wildlife in this area consists of mostly of Elephants (*Elephas maximus*), Spotted deer (*Axis axis*), Sambar (*Rusa unicolor*), Neelgai (*Boselaphus tragocamelus*) and langooors (*Simia entellus*). Tigers (*Panthera tigris*) have also been spotted occasionally. This area has a large elephant population, making it dangerous to explore thoroughly on foot.



## 4. MATERIALS AND METHODS

This chapter is divided into two parts. The first part is a brief description of the fieldwork and how the data collected in the field was used to calculate the tree height, stem volume and AGB for the Barkot Forest Area. The second portion consists of the PolInSAR techniques that were used to estimate stem volume, tree height and AGB.

Forty-five plots were used to collect field data. GPS locations of these plots were recorded. Coherence and backscatter values were extracted for these same locations and the results were compared.

### 4.1. Materials

#### 4.1.1. Satellite Data

An interferometric pair of fully polarimetric Radarsat-2 data was used. Table 4-1 displays the specifications of the data. The PolInSAR data pair was obtained with a gap of 24 days and was acquired in ‘Fine’ mode.

Table 4-1: Radarsat-2 Data. The information in the table was provided in the product file that came with the data. It can also be found at (<http://www.asc-csa.gc.ca/eng/satellites/radarsat2/>).

<b>Description</b>	<b>Image 1</b>	<b>Image 2</b>
<b>Satellite</b>	RADARSAT-2	RADARSAT-2
<b>Date of Acquisition</b>	4-Mar-13	28-Mar-13
<b>Time of Acquisition</b>	0:44:45	0:44:45
<b>Image Id</b>	246434	250469
<b>Acquisition mode</b>	Fine Quad-polarization	Fine Quad-polarization
<b>Wavelength (cm)</b>	5.55	5.55

#### 4.1.2. Field Data

Fieldwork was carried out in last weeks of November and December and first week of January 2014. The Barkot Forest Area mostly consists of mature Sal forests which means that the biomass of the area will not change drastically from year to year. Therefore collecting

field data in the winter of 2013 should not be a parameter that counts for significant deviation in AGB estimation, if any does occur.

A total of 45 plots were sampled in the Barkot Forest Area. A stratified sampling method was used in the collection of field data. The study area was stratified by forest type, using a preliminary photo interpretation method. The plots were square in shape with an area of 0.1 ha. Tree parameters such as height and circumference at breast height (CBH) were measured and stem volume and AGB were calculated for each plot. Fig. 4-1 illustrates the distribution of the sample plots. Most of the plots were set up in the Sal forest (27), 14 in the dry mixed miscellaneous and 4 in the Khair-Sissoo.

#### **4.1.3. Ancillary Data**

The stem volume from the field data (height, CBH, basal area) was calculated using volumetric equations from the Forest Survey of India [72] (Appendix. 1). The specific gravity values were taken from “The Specific Gravity: Indian Woods [73]”, and were used to calculate AGB from stem volume.

#### **Tools**

- A handheld Trimble Global Positioning System (GPS) with an accuracy ranging between 5-10 m was used to get a latitude/longitude reading of the sample plots. The readings were taken at the center of each plot.
- A compass was used to make sure that the plots were square in shape by. This was done by using the compass to align the corners of the plot correctly.
- A laser dendrometer, ‘Criterion RD 1000’ was used to measure tree heights (<http://www.lasertech.com/Criterion-RD-1000.aspx>).

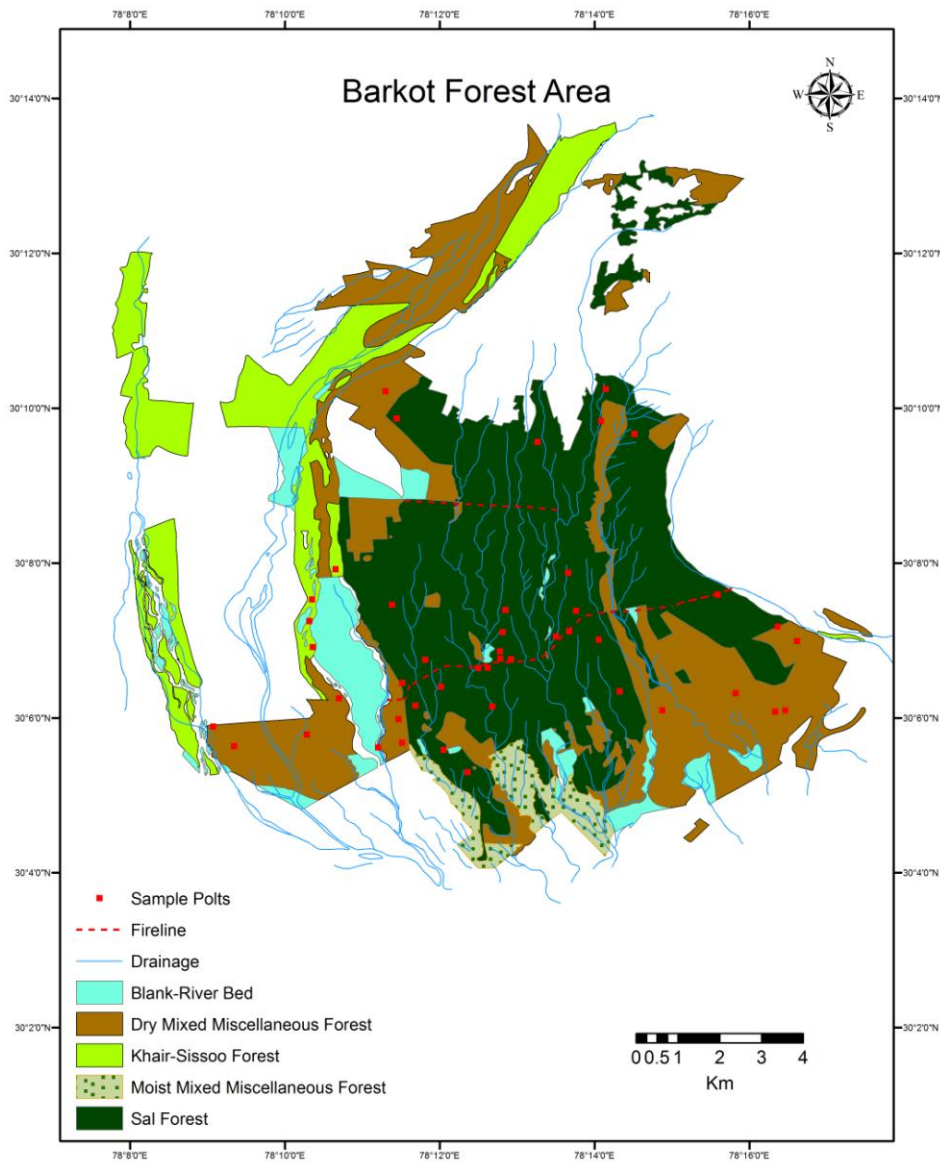


Figure 4-1: LULC Map of Barkot Forest Area. The area has been divided into dry mixed miscellaneous forest, Khair-Sissoo forest, moist mixed miscellaneous forest and Sal forest. The majority of the points lie within the Sal forest as it covers most of the Barkot Forest. Source: Forest Department, Uttarakhand, India

## 4.2. Methods

### 4.2.1. Fieldwork and calculations

Figure 4-2 shows the sample plots, which were square in shape and measured approximately 31 by 31m. In the field, CBH and tree height were measured for each tree in the sample plots. The CBH was converted to diameter at breast height (DBH) using the circumference formula (Eq.4-1). All of the trees in the plots were identified and their botanical as well as common names were noted. This was done with the help of the forest rangers.

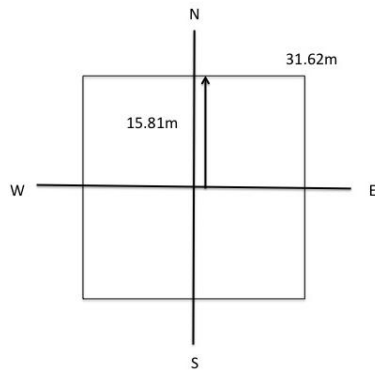


Figure 4-2: Sample plot

#### 4.2.2. Basal Area

The basal area of each tree in the sample plots was calculated using formula

$$A = \pi r^2 \quad (4-1)$$

Where,  $A$  is the basal area ( $m^2$ ) and  $r$  (m) is the radius of the tree in meters.

#### 4.2.3. Stem Volume

The stem volume was calculated using the species-specific volume equations from the Forest Survey of India [72] (Appendix 1). These equations require stem diameter. There were a few species for which these equations were not available and the quarter girth formula was used for these species.

$$V_{qg} = g^2 h = (\pi d)^2 h \quad (4-2)$$

Where  $V_{qg}$  is the stem volume,  $g$  refers to the circumference at breast height (also known as girth),  $d$  is the diameter of the tree and  $h$  the height.

#### 4.2.4. Aboveground Biomass Estimation (AGB)

The field AGB was calculated using stem volume, which has been calculated previously, and specific gravity values [73] (Appendix 2). Eq. 4-3 shows the formula that was used to calculate the AGB.

$$AGB = SV \times SG \quad (4-3)$$

Where  $SV$  is the stem volume ( $m^3$ ) and  $SG$  the specific gravity. Destructive sampling cannot be carried out in India and therefore the volumetric equations provided by the FSI and the

specific gravity values from the Indian Woods book [73] had to be used. The FSI did however use destructive sampling to get their values.

### 4.3. Methodology

The flow chart (Fig. 4-3) shows the steps that were taken in order to retrieve the needed parameters for IWCM modeling and its accuracy assessment.

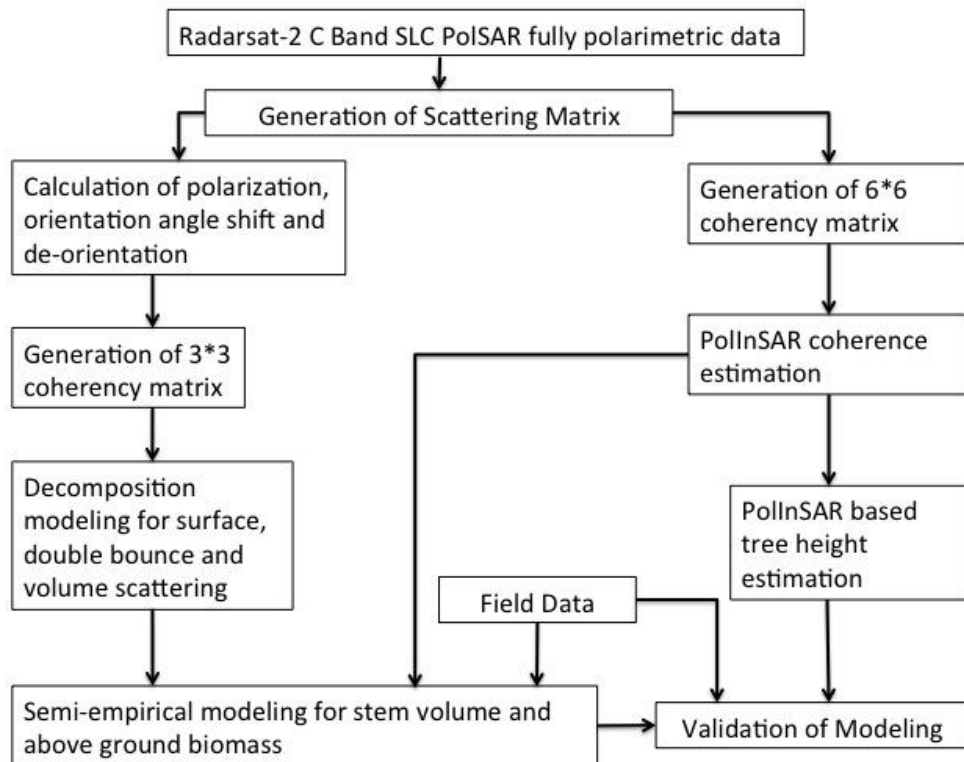


Figure 4-3: Methodology

### 4.4. PolInSAR based parameter retrieval and AGB estimation

#### 4.4.1. Polarimetric Decomposition

The decomposition of backscattered values allows for the backscattered signal to be segregated into surface scattering, double bounce and volume scattering and each has a certain physical significance. There are two types of decompositions, coherent decomposition and incoherent decomposition [30]. Coherent decomposition is not useful in retrieving information on natural mediums as they only describe the scattering that occurs from coherent or pure targets, therefore this thesis will focus on incoherent decomposition.

The incoherent decomposition technique uses the coherency matrix to separate the various scattering processes that are present in each pixel. The present study uses the four-component decomposition technique proposed by Yamaguchi et al. [49].

The first step was to generate a scattering matrix (refer to Eq. 2-1) from the single look complex (SLC) data. The scattering matrix presents the scattering characteristics of the target in the form of four polarization; HH, HV, VH and VV. The second step is to generate the coherency matrix [T] (refer to Eq. 2-2) by generating the vectorized form of the scattering matrix,  $k_p$ , (Eq.4-4) and multiplying it with its complex conjugate transpose ( $[T] = k_p \times k_p^\dagger$ ).

$$k_p = \frac{1}{\sqrt{2}} \begin{bmatrix} S_{HH} + S_{VV} \\ S_{HH} - S_{VV} \\ 2S_{HV} \end{bmatrix} \quad (4-4)$$

The Yamaguchi four-component model decomposes the coherency matrix [T] into four matrices corresponding to various scattering elements (Eq.4-5).

$$[T] = f_v [T]_{\text{volume}} + f_s [T]_{\text{surface}} + f_d [T]_{\text{double}} + f_c [T]_{\text{helix}} \quad (4-5)$$

Where  $f_v, f_s, f_d$  and  $f_c$  are expansion coefficients and  $[T]_{\text{volume}}, [T]_{\text{surface}}, [T]_{\text{double}}$  and  $[T]_{\text{helix}}$  are the matrices representing various scattering types (volume, surface, double and helix). Each of these matrices corresponds to a unique scattering mechanism [49].

The expansion coefficients can also be written in terms of scattering vector elements (Eq. 4-6).

$$f_v = 8 \langle |S_{HV}|^2 \rangle - 4 |Im \langle S_{HV}^* (S_{HH} - S_{VV}) \rangle| \quad (4-6)$$

$$f_s = B - \frac{|C|^2}{A}$$

$$f_d = \frac{1}{2} \langle |(S_{HH} - S_{VV})|^2 \rangle - 2 \langle |S_{HV}|^2 \rangle$$

$$f_c = 2 |Im \langle S_{HV}^* (S_{HH} - S_{VV}) \rangle|$$

Where,

$$A = \frac{1}{2} \langle |(S_{HH} - S_{VV})|^2 \rangle - 2 \langle |S_{HV}|^2 \rangle$$

$$B = \frac{1}{2} \langle |(S_{HH} + S_{VV})|^2 \rangle - 4 \langle |S_{HV}|^2 \rangle + 2 |Im \langle S_{HV}^* (S_{HH} - S_{VV}) \rangle|$$

$$C = \frac{1}{2} \langle (S_{HH} + S_{VV})(S_{HH} - S_{VV})^* \rangle$$

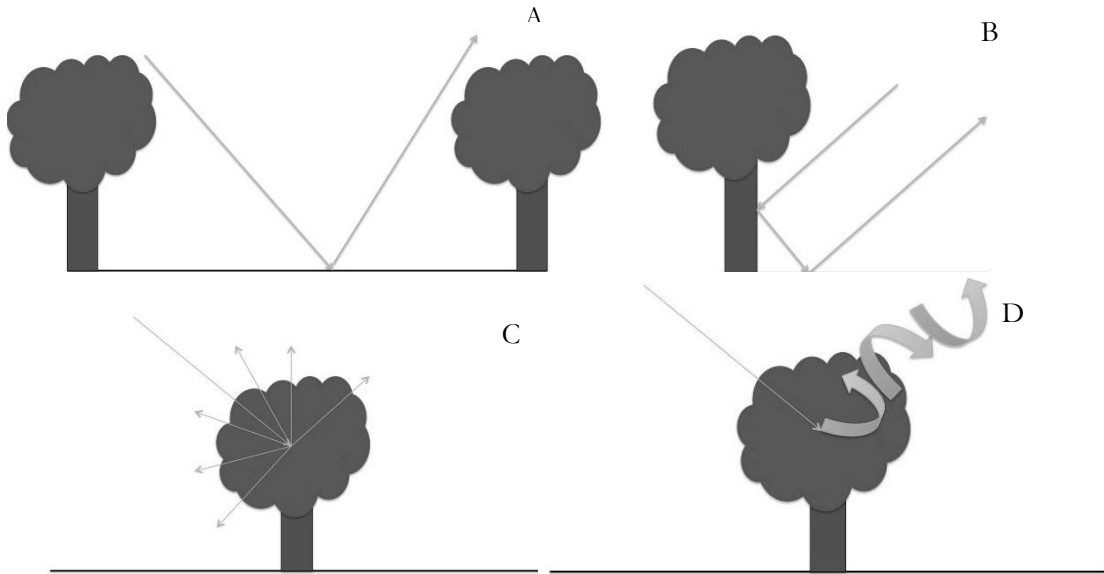


Figure 4-4: The image illustrates the four scattering mechanisms. A shows surface scattering, B double bounce, C volume and D shows helix scattering.

**i. Volume Scattering**

This type of scattering is typical of the vegetation and takes place in the canopy layer of the forest, from the leaves and the branches. The matrix (Eq. 4-7) presents the randomly oriented dipole and image ‘C’ in Fig. 4-4 is a representation of it.

$$[T]_{\text{volume}} = \frac{1}{4} \begin{bmatrix} 2 & 0 & 0 \\ 0 & 1 & 0 \\ 0 & 0 & 1 \end{bmatrix} \quad (4-7)$$

**ii. Surface Scattering**

Surface scattering is also known as single bounce. The matrix (Eq. 4-8) presents the model, while image ‘A’ in Fig. 4-4 depicts how surface scattering takes place in a forest.

$$[T]_{\text{surface}} = \frac{1}{4} \begin{bmatrix} 1 & \beta^* & 0 \\ \beta & \beta^2 & 0 \\ 0 & 0 & 0 \end{bmatrix} \quad (4-8)$$

Where  $\beta = \frac{R_h - R_v}{R_h + R_v}$ ,  $R_h$  and  $R_v$  are the horizontal and vertical polarized wave reflection coefficients.

**iii. Double bounce scattering**

Double bounce scattering results from corner reflectors. As image ‘B’ in Fig. 4-4

shows, the incident wave hits an object is reflected at a right angle and it hits another object and is reflected again. This sort of reflection is typical of corner reflectors and is associated with scattering that occurs due to stem-ground interactions. Eq. 4-9 presents double bounce in the form of a matrix.

$$[T]_{\text{double}} = \frac{1}{4} \begin{bmatrix} \alpha^2 & \alpha & 0 \\ \alpha^* & 1 & 0 \\ 0 & 0 & 0 \end{bmatrix} \quad (4-9)$$

#### iv. Helix Scattering

Helix scattering is the added scattering component in the Yamaguchi four-component modeling and is illustrated in image ‘D’ in Fig. 4-4.

$$[T]_{\text{helix}} = \frac{1}{2} \begin{bmatrix} 0 & 0 & 0 \\ 0 & 1 & \pm j \\ 0 & \pm j & 1 \end{bmatrix} \quad (4-10)$$

Using Equations (4-5) - (4-10) coherency matrix can be expressed as

$$[T] = \frac{f_v}{4} \begin{bmatrix} 2 & 0 & 0 \\ 0 & 1 & 0 \\ 0 & 0 & 1 \end{bmatrix} + \frac{f_s}{4} \begin{bmatrix} 1 & \beta^* & 0 \\ \beta & \beta^2 & 0 \\ 0 & 0 & 0 \end{bmatrix} + \frac{f_d}{4} \begin{bmatrix} \alpha^2 & \alpha & 0 \\ \alpha^* & 1 & 0 \\ 0 & 0 & 0 \end{bmatrix} + \frac{f_c}{2} \begin{bmatrix} 0 & 0 & 0 \\ 0 & 1 & \pm j \\ 0 & \pm j & 1 \end{bmatrix} \quad (4-11)$$

Here the total scattering power is  $P_t = P_s + P_d + P_v + P_c$

Where  $P_t$  is total power,  $P_s$  is power from surface scattering,  $P_d$  is double bounce,  $P_v$  is volume scattering and  $P_c$  is helix scattering. Helix scattering is not considered in this project as this term is added to model the scattering that appears in urban areas and is negligible for natural mediums [49]. The reason the four-component decomposition model was used is because it models volume scattering better than the three-component decomposition model.

#### 4.4.2. POLInSAR Satellite data processing

The PolInSAR processing of the data was done in several steps, which are described below.

- Generation of Master and Slave images
- Coregistration of Master and Slave images
- Baseline Estimation
- Interferogram Generation
- Flat Earth Removal
- Coherency matrix  $[T_6]$  Generation
- Coherence Estimation
- Vegetation Height Estimation

#### 4.4.2.1. Generation of Master and Slave images

A PolInSAR image is the combination of two polarimetric images using interferometry. These two images are combined to understand and manipulate the polarimetric and interferometric correlation that exists between the two images. The PolInSAR data pair are two images of the same area from different angles and two different time periods. Fig. 4-5 illustrates the PolInSAR geometry.

The first image, also known as the Master, is from 4<sup>th</sup> March 2014 and the second (Slave) is from 28<sup>th</sup> March 2014. The details of the images are listed in table 4-1. Eq. 4-12 and 4-13 are the images, presented in the form of scattering matrices.

$$[S_1] = \begin{bmatrix} S_{HH}^1 & S_{HV}^1 \\ S_{VH}^1 & S_{VV}^1 \end{bmatrix} \quad (4-12)$$

$$[S_2] = \begin{bmatrix} S_{HH}^2 & S_{HV}^2 \\ S_{VH}^2 & S_{VV}^2 \end{bmatrix} \quad (4-13)$$

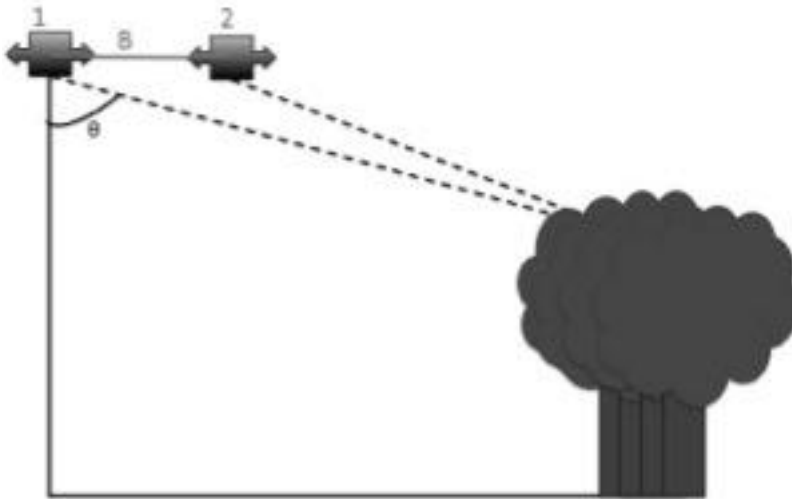


Figure 4-5: PolInSAR Geometry. B is the baseline distance between the two platforms (1 and 2) during the PolInSAR image acquisition and  $\theta$  is the angle of incidence.

#### 4.4.2.2. Co-registration of SLC master and slave track images

The first step in PolInSAR processing is co-registration as it links the two images and finds the overlapping area that they share. This step is necessary as it reduces the loss of coherence due to misalignment. Temporal decorrelation is caused due to changes in the time in which the two images were acquired and they lead to loss in coherence and need to be balanced.

#### 4.4.2.3. Baseline Estimation

Precise baseline estimations are vital to conversion of interferometric phase into surface

heights. Fig. 4-5 illustrates satellites 1 and 2 separated by the baseline B. Interferograms with small baselines cannot be used, as they are extremely sensitive to atmospheric effects and result in a high level of noise. The normal baseline should not exceed the critical baseline as coherence will be lost and interferogram cannot be generated. Table 4-2 shows the baseline information generated for this project.

Table -4-2: Baseline Information

Parameter	Value
Baseline	78m
Critical Baseline	3857.57m
Time Baseline	24 days
Range Shift	0.845 pixels
Azimuth Shift	88.33 pixels

#### 4.4.2.4. Interferogram Generation

An interferogram is produced through the multiplication of each pixel of the first image with the complex conjugate of the second image. The interferometric phase is a result of the difference in phase between image one and two and the amplitude is a product of the amplitude of the two images.

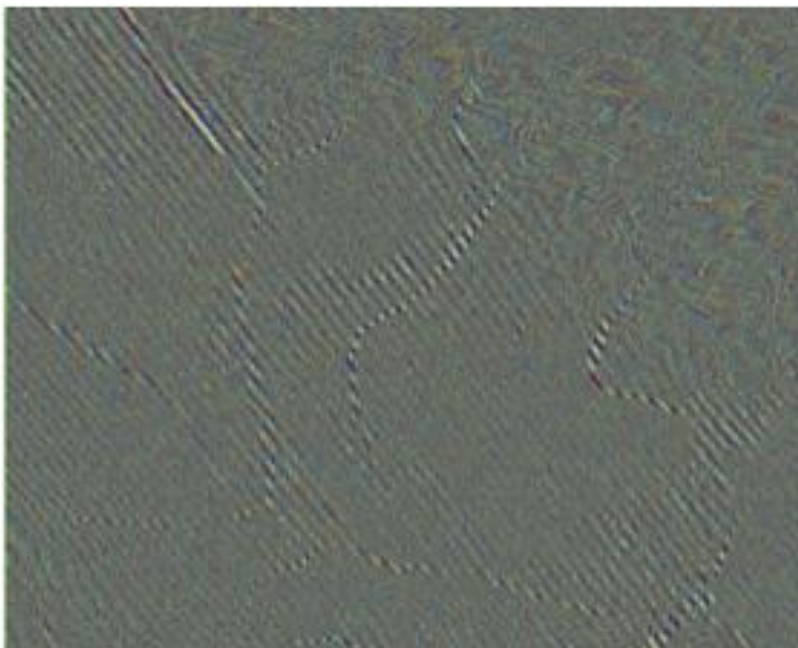


Figure 4-6: Interferogram of HV+VH

Fig. 4-6 shows the HV plus HV interferogram image of the Barkot forest area. There are two types of fringe patterns that can be observed in this image. The first are narrow, bright the fringes that appear vertically across the image and the second are the duller more spread out fringes that can be seen in the top right hand corner of the image. The vertical fringes represent the drainage present in the Barkot Forest Area and the fringes on the top right hand corner are present because that is where the Shivalik hills begin. Both types of fringes show change in elevation. The surface of the river, as it cuts through this terrain changes constantly and therefore change in elevation can be seen.

#### 4.4.2.5. Flat Earth Removal

Flat earth removal is carried out to remove the noise, which is contributed by phase variation. Interferometric phase difference is caused by phase difference due to terrain and by phase difference due to flat Earth. Flat Earth removal is carried out so that the interferogram should relate to the topography alone. According to Cloude [30] this variation in phase can be calculated using Eq. 4-14.

$$e^{i\phi_{fe}} = \exp\left(i\frac{4\pi}{\lambda}(r_2 - r_1)\right) \quad (4-14)$$

Where,

$$r_1 = \sqrt{(h^2 + y^2)}$$

$$r_2 = \sqrt{(h^2 + (y + B)^2)}$$

y = ground range co-ordinate

#### 4.4.2.6. Coherency Matrix [T<sub>6</sub>] Generation

The combination of two polarimetric images results in a PolInSAR image.  $K_{p1}$  and  $K_{p2}$  (Eq. (4.15)-(4-17)) are the vectorized form of the two scattering matrices used to create the coherency matrix (Eq. 4-18).

$$K_p = \begin{bmatrix} K_{p1} \\ K_{p2} \end{bmatrix} \quad (4-15)$$

$$K_{p1} = \begin{bmatrix} S_{HH}^1 + S_{VV}^1 \\ S_{HH}^1 - S_{VV}^1 \\ 2S_{HV}^1 \end{bmatrix} \quad (4-16)$$

$$K_{p2} = \begin{bmatrix} S_{HH}^2 + S_{VV}^2 \\ S_{HH}^2 - S_{VV}^2 \\ 2S_{HV}^2 \end{bmatrix} \quad (4-17)$$

$$[T_6] = \langle K_p K_p^\dagger \rangle = \begin{bmatrix} T_{11} & \Omega_{12}^\dagger \\ \Omega_{12} & T_{22} \end{bmatrix} \quad (4-18)$$

Where,

$$T_{11} = \langle K_{p1} K_{p1}^\dagger \rangle$$

$$T_{22} = \langle K_{p2} K_{p2}^\dagger \rangle$$

$$\Omega_{12} = \langle K_{p1} K_{p2}^\dagger \rangle$$

$$\Omega_{12}^\dagger = \langle K_{p2} K_{p1}^\dagger \rangle$$

$T_{11}$  and  $T_{22}$  are the polarimetric coherency matrices generated for images 1 and 2.  $\Omega_{12}$  and  $\Omega_{12}^\dagger$  are the cross-correlation matrices. These matrices describe the polarimetric and interferometric associations that exist between the two polarimetric images.

#### 4.4.2.7. Coherence Estimation

Fig. 4-7 shows a coherence image. The white portions have high coherence and the black portions have low coherence. Absolute coherence ( $\gamma$ ) measures the degree of coherence that exists in an interferogram and it ranges from 0 to 1, 0 being complete decorrelation and 1 being a pure target with complete coherence. To estimate this interferometric coherence unitary projection vectors,  $\omega_1$  and  $\omega_2$  were used.  $\omega_1$  equals to  $\omega_{pq}$  and  $\omega_2$  equals to  $\omega_{ab}$ ,  $pq$  and  $ab$  are the receive and transmit polarizations. Projection vectors are used to estimate the degree of coherence that exists between two images from different positions for the same feature.

Further, scalar scattering coefficients were generated using Eq. 4-19 [10].

$$\mu_1 = \omega_1^\dagger K_{p1}, \quad \mu_2 = \omega_2^\dagger K_{p2} \quad (4-19)$$

$\mu_1$  and  $\mu_2$  are basically linear combinations of the scattering matrices  $[S_1]$  and  $[S_2]$ . The  $\dagger$  represents transpose of the matrix. An interferogram was then generated using the linear combinations relating them to the unitary projection vectors as shown in Eq.4-20.

$$\mu_1 \mu_2^\dagger = \langle \omega_1^\dagger K_{p1} K_{p2}^\dagger \omega_2 \rangle = \omega_1^\dagger \Omega_{12} \omega_2 \quad (4-20)$$

Complex coherence is the vectorized form of scalar interferometric coherence [9]. Eq.4-21 illustrates how complex coherence can be calculated for different polarization combinations.

$$\gamma = |\gamma|e^{i\phi} = \gamma_{(\omega_1\omega_2)}$$

$$\gamma_{(\omega_1\omega_2)} = \frac{\langle \mu_1 \mu_2^\dagger \rangle}{\sqrt{\langle \mu_1 \mu_1^\dagger \rangle \langle \mu_2 \mu_2^\dagger \rangle}} = \frac{\omega_1^\dagger \Omega_{12} \omega_2}{\sqrt{\omega_1^\dagger T_{11} \omega_1 \omega_2^\dagger T_{22} \omega_2}} \quad (4-21)$$

Coherence generated from Eq. 4-21 is in complex form and therefore the magnitude of coherence was extracted using the amplitude images using the following formula (Eq.4-22).

$$Amplitude (A) = \sqrt{real\ component^2 + imaginary\ component^2} \quad (4-22)$$

Coherence values extracted from images using Eq.4-22 were used for semi-empirical modeling.

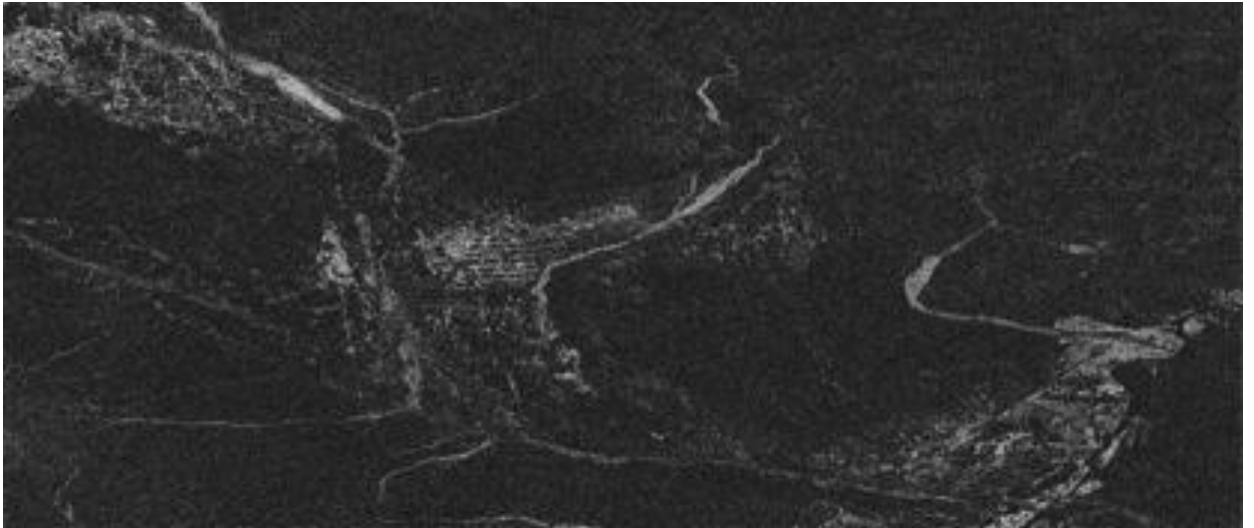


Figure 4-7: Coherence Image

#### 4.4.2.8. PolInSAR Height Estimation

The tree height was modeled using forest height inversion algorithm. The process is defined in detail in Chapter 5.

## 5. COHERENCE BASED, SEMI-EMPIRICAL MODEL

This chapter describes the Interferometric Water Cloud Model (IWCM), which is a coherence based semi-empirical model used for estimating forest biophysical parameters [11]. The parameters for this model were retrieved using field data and PolInSAR processed data. The chapter also discusses the accuracy of the model in forest biophysical parameter estimation. It further considers the forest height inversion algorithm, which is used for PolInSAR height estimation.

The input parameters for the IWCM were total backscatter ( $\sigma_{total}^0$ ), backscatter from vegetation ( $\sigma_{veg}^0$ ), backscatter from the ground ( $\sigma_{gr}^0$ ), total coherence ( $\gamma_{total}$ ), coherence from vegetation ( $\Gamma_{veg}$ ), coherence from ground ( $\Gamma_{gr}$ ) and semi-empirically defined coefficient  $\beta$ . From these parameters,  $\beta$  was unknown and was estimated using the average biomass of 10 sample plots. These sample plots were not used in the estimation of the modeled AGB.

The model was first proposed by Askne *et al.* and Santoro *et al.* [74],[28]. In their study they retrieved backscatter and coherence using single polarized data and had to estimate the various model parameters. This project focuses on the retrieval of coherence and backscatter from fully polarimetric data which makes the estimation of parameters much more accurate as all coherence and backscattering parameters can be extracted from the data itself and do not need to be estimated using regression techniques. The use of fully polarimetric data reduces the ambiguity in modeling the IWCM.

### 5.1. Model based parameter retrieval

Total forest backscatter is the sum of total backscatter from each pixel and total backscatter information can be obtained from a span image, which contains the sum of all types of scattering (single, double bounce and volume). Likewise, total forest coherence or complex forest coherence is also the sum of the coherence from vegetation and coherence from ground as these types of scattering take place in the vegetation. Other parameters required for modeling AGB, SV and tree height are transmissivity (T), vertical wave number ( $K_z$ ), attenuation ( $\sigma$ ) and empirically defined coefficient ( $\beta$ ).

#### 5.1.1. Transmissivity

Transmissivity (T) is the quantifiable evaluation of the ability of EM waves to transfer in and out of gaps in the canopy. The transmissivity depends on the amount of ground backscatter coming through the canopy. In a dense forest, the amount of ground scattering will be reduced as compared to an open forest and therefore the transmissivity of a dense forest will be considered low. Wavelength is also a deciding factor in transmissivity evaluation. The longer the wavelength, the higher will be the transmissivity. Praks *et al.* [75] expressed it as Eq.5-1.

$$T = \frac{\beta_{gc}}{\beta_{g0}} \quad (5-1)$$

Where,  $\beta_{gc}$  is the coefficient from ground scattering that is measured in the presence of an attenuating layer and  $\beta_{g0}$  is the ground scattering coefficient measured without canopy attenuation.

### 5.1.2. Two-way attenuation

The attenuation ( $\sigma$ ) communicates the degree to which the EM wave diminishes when it transmits through the canopy and the gaps in the canopy. Being a function of transmissivity attenuation can be written as Eq. 5-2 [75]

$$\sigma = \ln T \frac{\cos\theta}{-2h} \quad (5-2)$$

Where, T refers to the transmissivity,  $\theta$  is the incidence angle and h is the average tree height for each plot in the field. The incidence angles for the slave and the master images are averaged in order to take into consideration the effect of the incidence angle from both the images.

### 5.1.3. Vertical Wave Number

The vertical wave number ( $K_z$ ) calculates the interferogram's sensitivity to the variations in height. When height is calculated from the interferogram,  $K_z$  acts as the scaling factor and it can be calculated using averaged incidence angle and the wavelength of the data as seen in Eq. 5-3.

$$K_z = \frac{4\pi\Delta\theta}{\lambda\sin\theta} \quad (5-3)$$

### 5.1.4. Semi-empirically Defined Coefficient

The empirically defined coefficient ( $\beta$ ) can be calculated from the decomposition of the master and the slave images using the Eq. 5-4.

$$\beta = -\frac{1}{B_{AGB}} \ln \left[ \left( \frac{\sigma_{total}^0 - \sigma_{veg}^0}{\sigma_{gr}^0 - \sigma_{veg}^0} \right) \right] \quad (5-4)$$

Where is  $B_{AGB}$  is the average AGB of 10 plots from field data,  $\sigma_{total}^0$  is the total backscatter from surface, volume and double bounce scattering,  $\sigma_{veg}^0$  is the backscatter from vegetation that consists of backscatter from double bounce and volume and  $\sigma_{gr}^0$  is the backscatter from ground (surface scattering). Coherence from vegetation ( $\gamma_{veg}$ ) is the sum of coherence from volume and coherence from double bounce. The derivation of  $\beta$  is specified in Eq. 5-17.

### 5.1.5. Modeled Tree Height Estimation

This project focuses on estimating height using the height inversion algorithm, ‘height from coherence amplitude’ (HCA), given by Cloude and Papathanassiou [59]. In areas with low coherence, it is difficult to determine the height for a given point, as more than two heights can be estimated for the same point. To avoid such errors both solutions for height must be identified and the ambiguous height point should be ignored.

This is done by ignoring the phase and concentrating on the coherence amplitude only. In this algorithm it is necessary to choose a polarization channel that will have the smallest surface to volume scattering ratio. HV is the optimal choice for this as it’s surface to volume scattering ratio is the smallest. Height is estimated by comparing the amplitude of the chosen channel (HV) with random volume.

## 5.2. Water Cloud Model (WCM)

The WCM defines the backscatter from various forest biophysical scatterers and models total forest backscatter ( $\sigma_{total}^0$ ) as a sum of backscatter from vegetation ( $\sigma_{veg}^0$ ) and backscatter from the ground ( $\sigma_{gr}^0$ ). This research has considered backscatter from vegetation as a sum of volume scattering and double bounce scattering as they both result from canopy interactions while backscatter from the ground is just from the surface.

According to Leeuwen [76], the WCM can be simply written as

$$\sigma_{total}^0 = \sigma_{veg}^0 + \sigma_{gr}^0 T_{tree} \quad (5-5)$$

Where  $T_{tree}$  is transmissivity, which is the measured ability of the canopy to transmit the EM wave.

Askne et al. [74], developed the model further by introducing the area fill factor ( $\mu$ ) which, represents the canopy by taking into account the scattering that comes through the gaps in the canopy and the scattering that is attenuated by the canopy (Eq.5-6).

$$\mu = \frac{1 - e^{-\beta B_{AGB}}}{1 - e^{-\sigma h}} \quad (5-6)$$

Where  $e^{-\beta B_{AGB}} = T_{for}$  and  $e^{-\sigma h} = T_{tree}$  represent transmissivity of the forest and of a tree, respectively.

Therefore, Eq. 5-5 can be rewritten as

$$\sigma_{total}^0 = (1 - \mu)\sigma_{gr}^0 + \mu[\sigma_{gr}^0 T_{tree} + \sigma_{veg}^0 (1 - T_{tree})] \quad (5-7)$$

$T_{tree}$  can be written in terms of attenuation ( $\sigma$ ) (db/m) (which is explained in detail under IWCM) and attenuating height ( $h$ ) (m) as Eq. 5-8. This height ( $h$ ) represents the thickness of the attenuating layer and is also recognized as tree height. Eq.5-9 is total

backscatter described in terms of attenuation.

$$T_{tree} = e^{-\sigma h} \quad (5-8)$$

$$\sigma_{total}^0 = (1 - \mu)\sigma_{gr}^0 + \mu[\sigma_{gr}^0 e^{-\sigma h} + \sigma_{veg}^0 (1 - e^{-\sigma h})] \quad (5-9)$$

This Eq.5-9 can also be written as Eq.5-10.

$$\sigma_{total}^0 = [(1 - \mu) + \mu e^{-\sigma h}]\sigma_{gr}^0 + \mu\sigma_{veg}^0 (1 - e^{-\sigma h}) \quad (5-10)$$

Each pixel of the Radarsat-2 SAR image covers an area of 10m×10m, thereby making it extremely difficult to retrieve the transmissivity of a single tree, which is why the transmissivity of the forest patch is considered. Thus  $T_{tree}$  is expressed as  $T_{for}$  and can be stated as a function of the fill factor ( $\mu$ ) [11].

$$T_{for} = [(1 - \mu) + \mu e^{-\sigma h}] \quad (5-11)$$

Eq.5-11 can also be approximated to Eq.5-12 considering strong attenuation ( $\sigma$ ).

$$T_{for} = [(1 - \mu) + \mu e^{-\sigma h}] \approx (1 - \mu) \quad (5-12)$$

Substituting the Eq.5-12 in Eq.5-10, it can be written in terms of total backscatter as Eq.5-13

$$\sigma_{total}^0 = T_{for} \sigma_{gr}^0 + \sigma_{veg}^0 (1 - T_{for}) \quad (5-13)$$

Therefore Eq. 5-6 can be written as Eq. 5-14,

$$\mu = 1 - e^{-\beta B_{AGB}} \quad (5-14)$$

As  $(1 - e^{-\sigma h})$  can be ignored because of strong attenuation ( $\sigma$ ), which results in a large  $\sigma$ . So from equations 5-12 and 5-14 we get Eq 5-15 [77]

$$T_{for} = e^{-\beta B_{AGB}} \quad (5-15)$$

Using Eq.5-15, Eq. 5-13 can be written as Eq. 5-16

$$\sigma_{total}^0 = \sigma_{gr}^0 e^{-\beta B_{AGB}} + \sigma_{veg}^0 (1 - e^{-\beta B_{AGB}}) \quad (5-16)$$

Simplifying Eq. 5-16 to derive  $\beta$

$$\beta = -\frac{1}{B_{AGB}} \ln \left[ \left( \frac{\sigma_{total}^0 - \sigma_{veg}^0}{\sigma_{gr}^0 - \sigma_{veg}^0} \right) \right] \quad (5-17)$$

Eq.5-17 provides the value of the semi-empirically defined coefficient ( $\beta$ ).

### 5.3. Interferometric Water Cloud Model (IWCM)

The IWCM represents total coherence ( $\gamma_{total}$ ) and total backscatter ( $\sigma_{total}^0$ ) as the sum of backscatter and coherence contributed from the ground and from the vegetation as presented in Eq.5-18 and Eq.5-19 [78].

$$\Gamma_{gr} = (1 - \mu)\gamma_{gr} \left( \frac{\sigma_{gr}^0}{\sigma_{total}^0} \right) + \mu\gamma_{gr} T_{tree} \left( \frac{\sigma_{gr}^0}{\sigma_{total}^0} \right) \quad (5-18)$$

$$\Gamma_{veg} = \mu\gamma_{veg} \left( \frac{\sigma}{\sigma - jk_z} \right) \left( \frac{\sigma_{veg}^0}{\sigma_{total}^0} \right) \{e^{-jk_z} - T_{tree}\} \quad (5-19)$$

Hence the IWCM can be written as Eq.5-20.

$$\begin{aligned} \gamma_{total} = & (1 - \mu)\gamma_{gr} \left( \frac{\sigma_{gr}^0}{\sigma_{total}^0} \right) + \mu\gamma_{gr} T_{tree} \left( \frac{\sigma_{gr}^0}{\sigma_{total}^0} \right) \\ & + \mu\gamma_{veg} \left( \frac{\sigma}{\sigma - jk_z} \right) \left( \frac{\sigma_{veg}^0}{\sigma_{total}^0} \right) \{e^{-jk_z} - T_{tree}\} \end{aligned} \quad (5-20)$$

Where,

$\mu$  is the areal fill factor

$(1 - \mu)\gamma_{gr}$  is the coherence from ground through the gaps in the canopy

$\mu\gamma_{gr}\Gamma_{veg}$  is the coherence from ground with attenuation from the canopy

$\gamma_{gr}$  and  $\gamma_{veg}$  are coherence from ground and vegetation,

$\sigma_{gr}^0$  and  $\sigma_{veg}^0$  are backscatter from ground and vegetation

$k_z$  is the vertical wave number that is described in detail under model parameters (Eq.5-3)

Equations 5-18 and 5-19 can also be written in terms of attenuation ( $\sigma$ ) and the thickness of the attenuating layer ( $h$ ) as equations 5-21 and 5-22.

$$\Gamma_{gr} = (1 - \mu)\gamma_{gr} \left( \frac{\sigma_{gr}^0}{\sigma_{total}^0} \right) + \mu\gamma_{gr} e^{-\sigma h} \left( \frac{\sigma_{gr}^0}{\sigma_{total}^0} \right) \quad (5-21)$$

$$\Gamma_{veg} = \mu\gamma_{veg} \left( \frac{\sigma}{\sigma - jk_z} \right) \left( \frac{\sigma_{veg}^0}{\sigma_{total}^0} \right) \{e^{-jk_z} - e^{-\sigma h}\} \quad (5-22)$$

In Eq. 5-22, volume decorrelation  $\{e^{-jk_z} - e^{-\sigma h}\}$  is a resultant of the scattering that takes places due to attenuation ( $\sigma$ ) and height ( $h$ )[17]. An EM wave consists of amplitude

information and phase information that can be written as  $A \times \exp(j\phi)$ , where  $A$  represents the amplitude and  $\phi$ , the phase. These components can further be written as Eq. 5-23.

$$A \times \exp(j\phi) = \left\{ \frac{\sigma^2}{\sigma^2 + k_z^2} \right\} \exp\left(j \tan^{-1}\left(\frac{k_z}{\sigma}\right)\right) \quad (5-23)$$

Based on Eq. 5-23, Eq.5-22 can be written as Eq.5-24

$$\Gamma_{veg} = \mu \gamma_{veg} \left( \frac{\sigma_{veg}^0}{\sigma_{total}^0} \right) \left\{ \frac{\sigma^2}{\sigma^2 + k_z^2} \right\} \exp\left(j \tan^{-1}\left(\frac{k_z}{\sigma}\right)\right) (e^{-jk_z} - e^{-\sigma h}) \quad (5-24)$$

C-band is high in frequency with a shorter wavelength as compared to L and P bands; therefore the transmissivity can be neglected. Using this and the Taylor series expansion  $\left(\tan^{-1}\left(\frac{k_z}{\sigma}\right)\right)$  Eq. (5-21) and (5-24) can be written as Eq. (5-25) and (5-26).

$$\Gamma_{gr} = (1 - \mu) \gamma_{gr} \left( \frac{\sigma_{gr}^0}{\sigma_{total}^0} \right) \quad (5-25)$$

$$\Gamma_{veg} = \mu \gamma_{veg} \left( \frac{\sigma_{veg}^0}{\sigma_{total}^0} \right) (e^{-jk_z(h - \sigma^{-1})}) \quad (5-26)$$

Using Eq. (5-17), (5-25) and (5-26), the total forest coherence ( $\gamma_{total}$ ) can be written as Eq. 5-27.

$$\begin{aligned} \gamma_{total} = e^{-\beta B_{AGB}} & \gamma_{gr} \left( \frac{\sigma_{gr}^0}{\sigma_{total}^0} \right) \\ & + \left[ \left( (1 - e^{-\beta B_{AGB}}) \gamma_{veg} \left( \frac{\sigma_{veg}^0}{\sigma_{total}^0} \right) (e^{-jk_z(h_{modeled} - \sigma^{-1})}) \right) \right] \end{aligned} \quad (5-27)$$

To estimate AGB for each plot, Eq. 5-27 can be written as Eq. 5-28.

$$B_{AGB} = -\frac{1}{\beta} \left[ \ln \left\{ \frac{\gamma_{total} - \gamma_{veg} \left( \frac{\sigma_{veg}^0}{\sigma_{total}^0} \right)}{\gamma_{gr} \left( \frac{\sigma_{gr}^0}{\sigma_{total}^0} \right) - \gamma_{veg} \left( \frac{\sigma_{veg}^0}{\sigma_{total}^0} \right)} \right\} \right] \quad (5-28)$$

The AGB for each plot can be estimated using beta coefficient, coherence from ground and vegetation and backscatter from vegetation and ground.

## 5.4. Performance Analysis of Modeled Parameters

The precision of the model-derived parameters was tested using three methods; Root Mean Square Error (RMSE) estimation, Coefficient of Determination ( $R^2$ ) and Percent Accuracy.

### 5.4.1. Root Mean Square Error (RMSE)

This method estimates error by calculating the difference between values obtained from modeling and the values measured in the field. Lower RMSE values mean high model reliability. The RMSE can be calculated using Eq. 5-29.

$$RMSE = \sqrt{\frac{\sum_{i=1}^N (P_i^{\text{modeled}} - P_i^{\text{measured}})^2}{N}} \quad (5-29)$$

Where  $N$  is the number of plots that were collected in the field,  $P_i^{\text{modeled}}$  are the model derived parameters and  $P_i^{\text{measured}}$  are the parameters measured in the field.

### 5.4.2. Coefficient of Determination

Coefficient of determination is judged as the degree to which two sets of numbers relate to each other statistically. This method is used to assess the trend between variables and evaluates how closely the data relates to the line of best fit. The coefficient of determination ( $R^2$ ) has a range from 0 to 1, the former being representative of no relationship and 1 illustrates the optimal line of best fit while non-linear relations may have negative values.

### 5.4.3. Percent Accuracy

The percent accuracy is calculated using Eq. 5-30 [79]

$$Accuracy (\%) = \left[ 1 - \frac{\sqrt{\frac{1}{N} \sum_{i=1}^N (P_i^{\text{modeled}} - P_i^{\text{measured}})^2}}{P_i^{\text{measured}}} \right] \times 100 \quad (5-30)$$

The accuracy of the modeled parameters expresses the applicability of the modeling technique in a reliable manner as it shows how closely the model estimated parameter (height and biomass) follows the field-measured parameter.



## 6. RESULTS

This chapter presents the results and is divided into two sections with the first section being a brief summary of the results that were obtained using field data. The second portion being the parameters obtained using PolInSAR coherence estimation. The two biophysical parameters obtained were height and AGB. AGB was estimated using semi-empirical modeling (IWCM) and coherence amplitude was used for modeling height. The accuracy assessment for the parameters has been done using field data for comparison. The biomass, volume and height have been given in terms of ( $\text{t ha}^{-1}$ ) (units per hectare) and a hectare is equal to  $10000 \text{ m}^2$ .

### 6.1. Fieldwork Results

The basal area, stem volume and AGB have been calculated for each plot using field measurements like height and CBH. The field measured height ranges from 14.3 m to 33m, with the average height being 21.20m. The SV ranges from 17.5 to  $51.57(\text{m}^3\text{ha}^{-1})$ , with an average of  $34.5 (\text{m}^3\text{ha}^{-1})$ . The field measured AGB ranges from 112.58 to  $356.06 (\text{t ha}^{-1})$  with an average of  $227.18 (\text{t ha}^{-1})$ .

### 6.2. Polarization Orientation Angle Shift

Eq. 2-3 was used to compensate the polarization orientation angle shift from the scattering matrix. Figures (6-1) and (6-2) illustrate the volume scattering for each plot, before and after deorientation, for the first date of acquisition (4th March 2013). Figures (6-4) and (6-5) show the same for the second date of acquisition (24th March 2013). The compensation for polarization orientation angle shift is depicted in Figures (6-3) and (6-6), where the values of volume scattering show a decline following deorientation. The blue line shows the volume scattering values after deorientation and the red line shows the volume scattering values before deorientation. The decline in the values depicted by the blue lines shows the reduction in the overestimation of volume scattering. The double bounce increases slightly and surface scattering shows no change in value after deorientation.

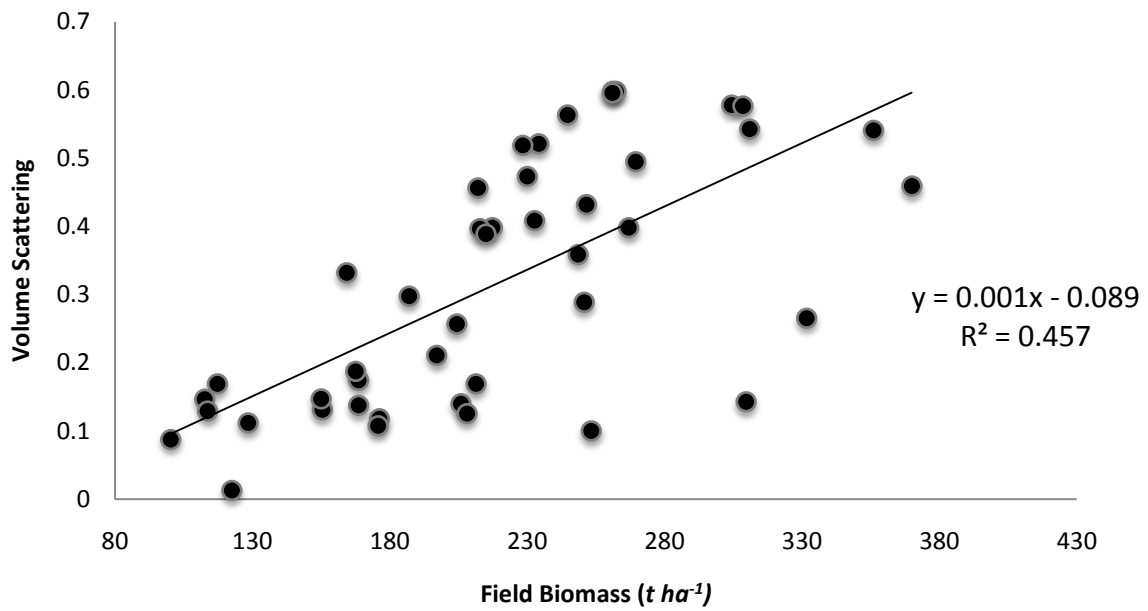


Figure 6-1: Volume scattering vs. field-calculated biomass for Master image (4<sup>th</sup> March, 2013), before deorientation. The volume scattering values increase with an increase in biomass.

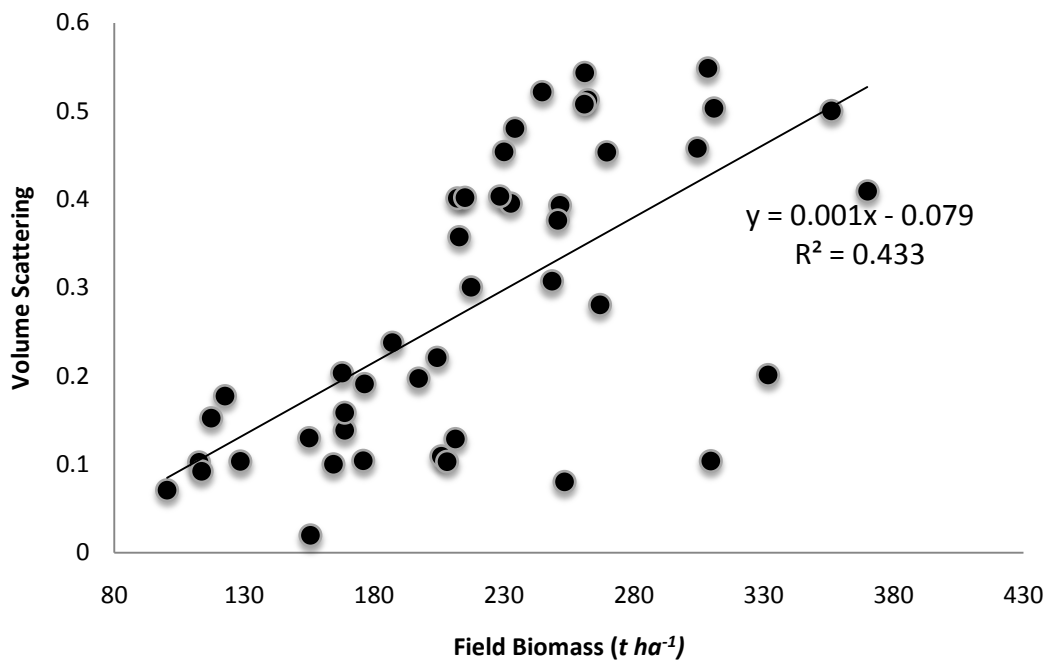


Figure 6-2: Volume scattering vs. field-calculated biomass for Master image (4<sup>th</sup> March, 2013) after deorientation. The volume scattering values increase with an increase in biomass. A decline in volume scattering values can be seen after deorientation.

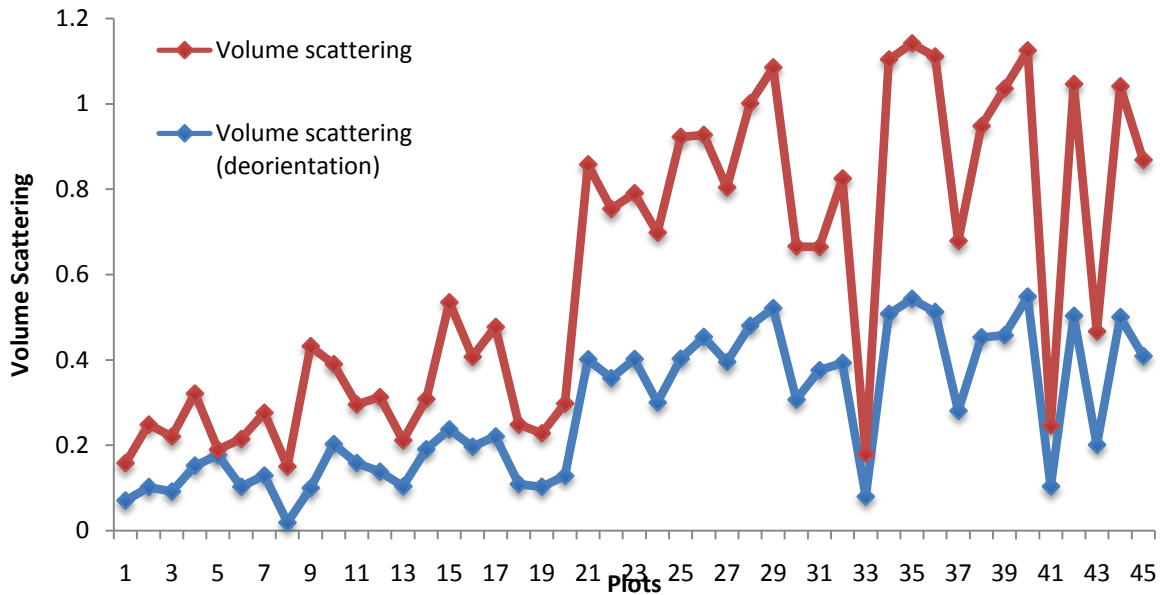


Figure 6-3: Difference in values of the volume backscattering before and after deorientation for Master image. The red line illustrates volume scattering values before deorientation and the blue line shows volume scattering values after deorientation.

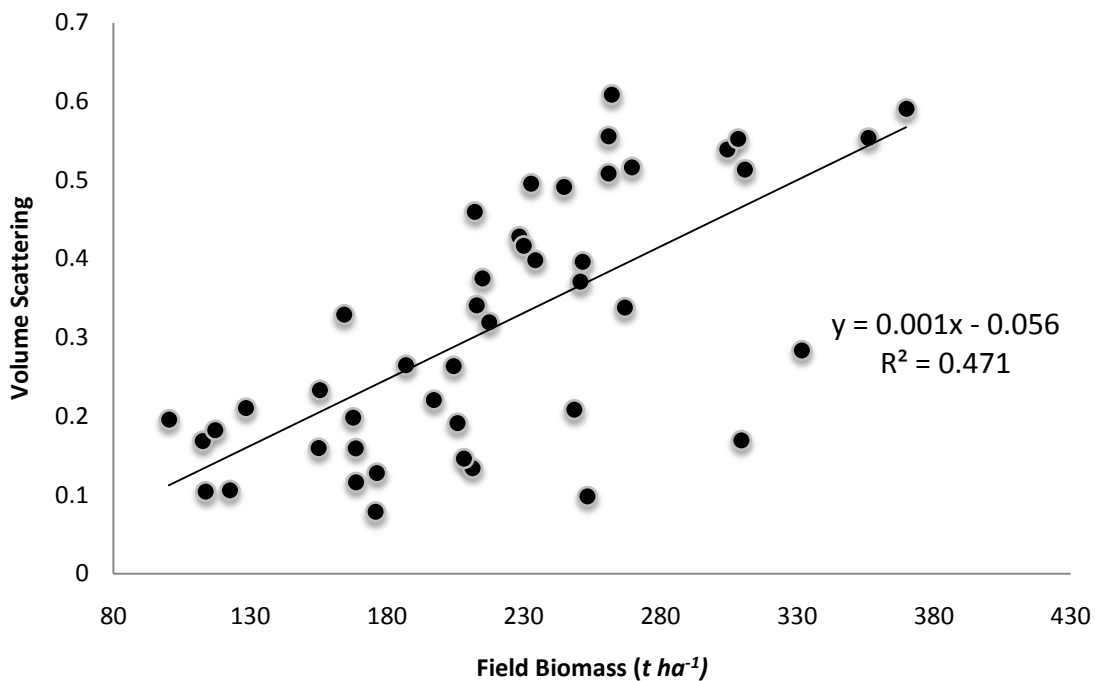


Figure 6-4: Volume scattering vs. field calculated biomass for Slave image (28<sup>th</sup> March, 2013) before deorientation. The volume scattering values increase with an increase in biomass.

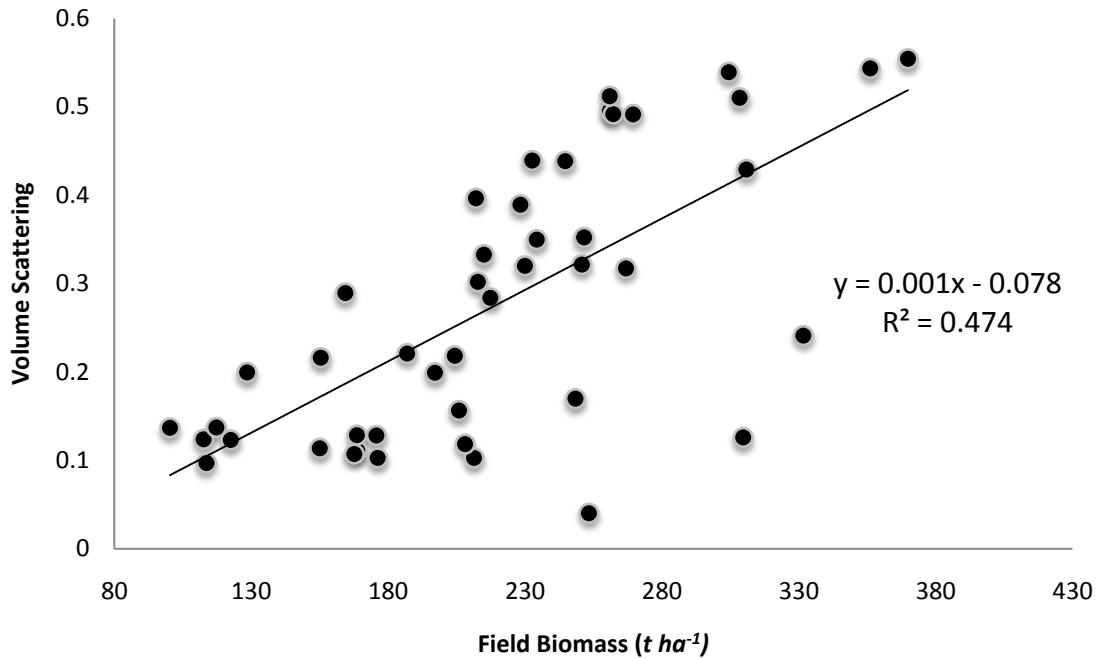


Figure 6-5: Volume scattering vs. field calculated biomass for Slave image (28<sup>th</sup> March, 2013) after deorientation. The volume scattering values increase with an increase in biomass. A decline in volume scattering values can be seen after deorientation

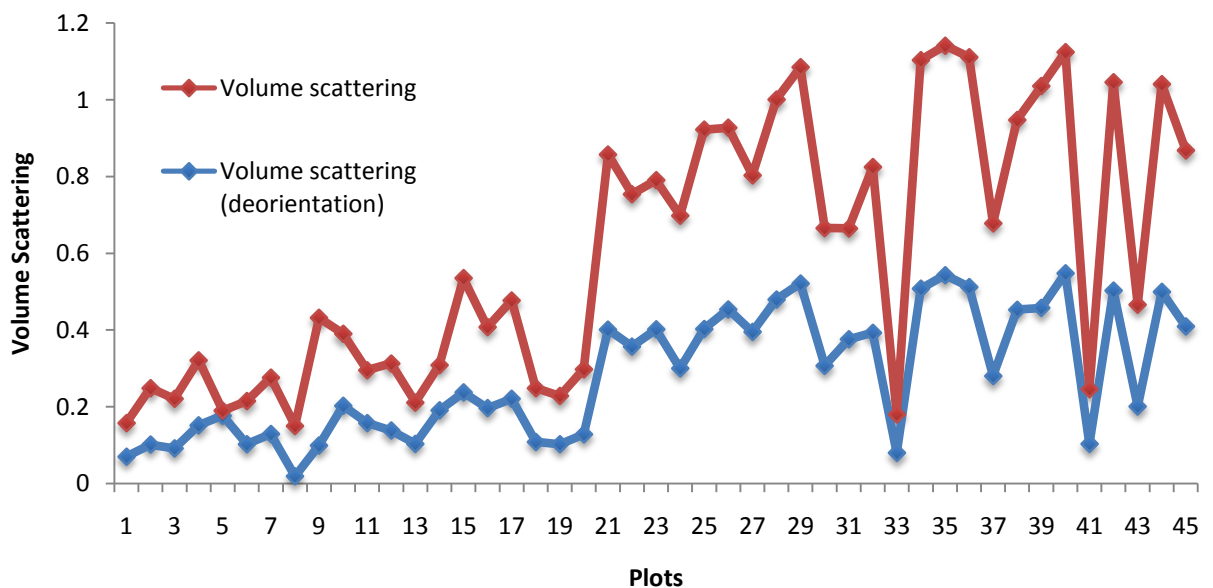
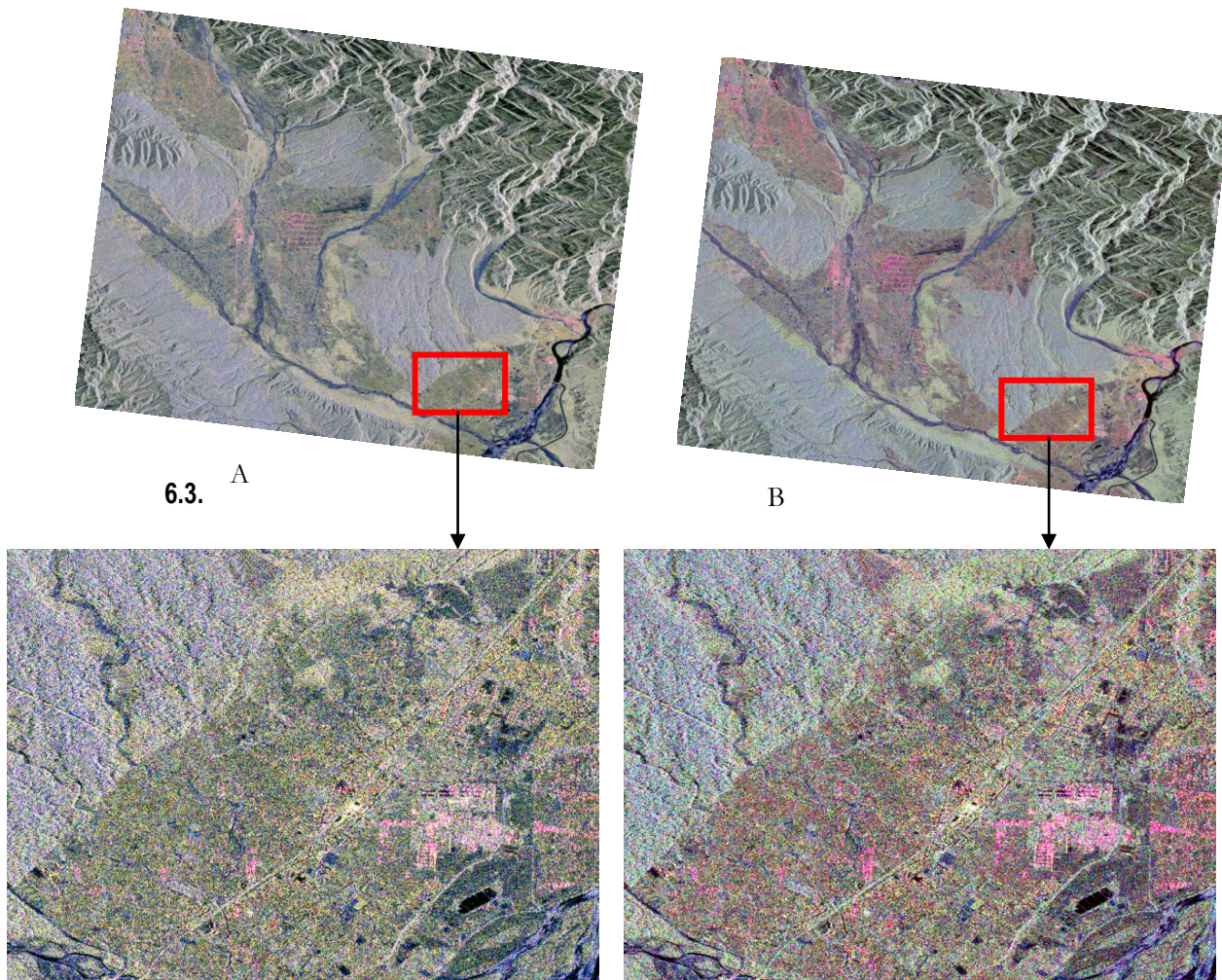


Figure 6-6: Difference in volume scattering values before and after deorientation for Slave image. The red line illustrates volume scattering values before deorientation and the blue line shows volume scattering values after deorientation.

The average value of volume scattering for the Master image declines from 0.318 to 0.28 after deorientation. The Slave image for 24<sup>th</sup> March 2013 also shows a decline in the average volume scattering values after deorientation, which reduces from 0.313 to 0.275.



6.3. A

B

Figure 6-7: Effect of polarization orientation angle shift and deorientation. Image A shows overestimated volume scattering, which has been compensated in Image B.

## Parameter Estimation

### 6.3.1. Forest Backscatter

The relationship between total forest backscatter ( $\sigma_{\text{total}}^0$ ) and biomass calculated from field data is shown in Figures (6-8) and (6-9). The  $R^2$  value (0.46) for the master image is more than the  $R^2$  value (0.24) for the Slave. The Master image from 4th March 2013 has been chosen as input parameter in IWCM modeling because the correlation between total backscatter and biomass is higher in the Master image.

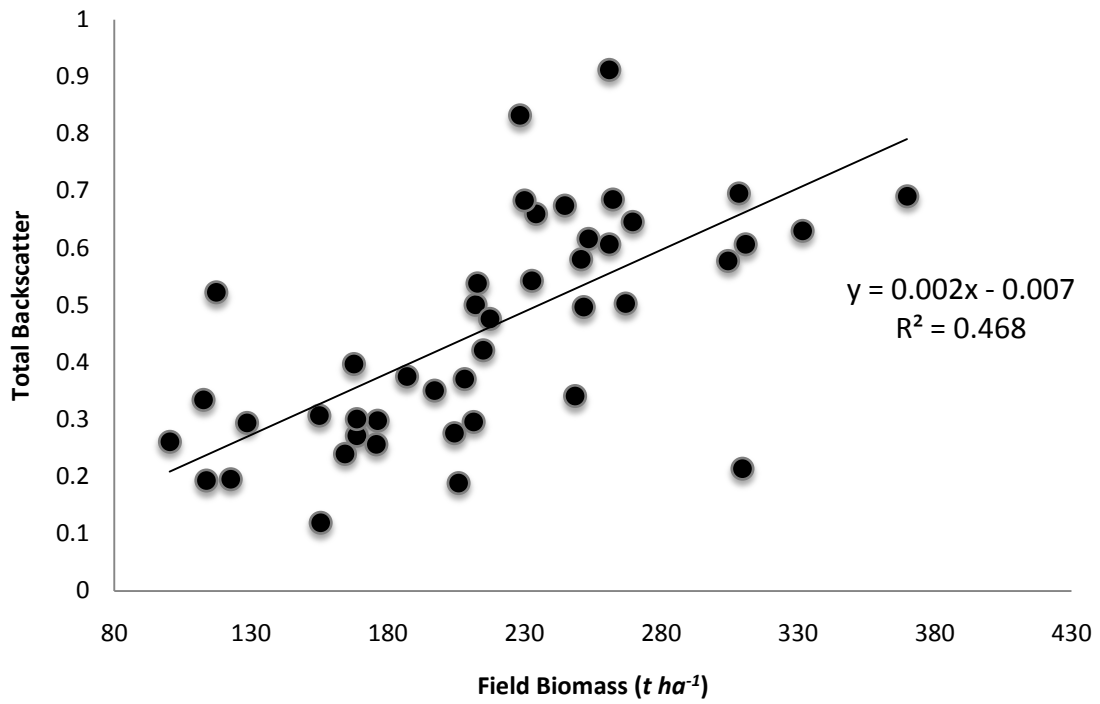


Figure 6-8: Total forest backscatter vs. biomass for the Master image. The correlation between biomass and backscatter values is higher in the master image.

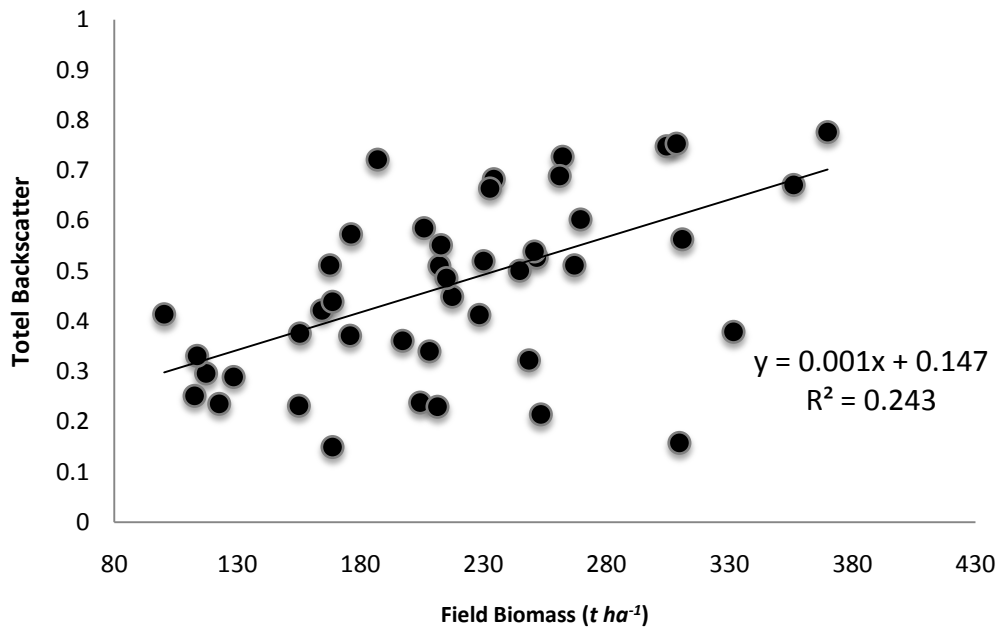


Figure 6-9: Total forest backscatter vs. biomass for the Slave image. The correlation between biomass and backscatter values is higher in the master image.

### 6.3.2. PolInSAR Coherence Estimation

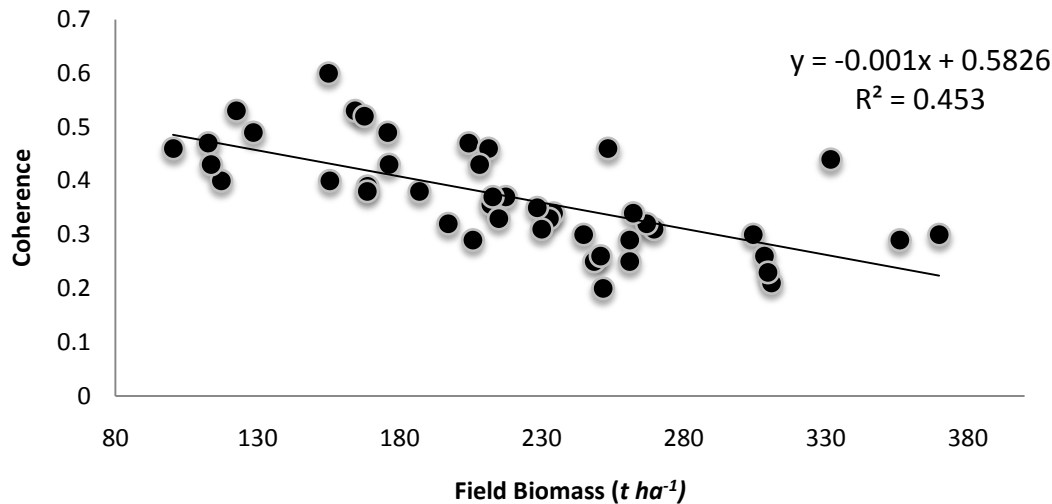


Figure 6-10: Total coherence vs. field biomass. The coherence decreases with an increase in biomass.

The  $R^2$  value for total coherence and biomass is 0.453 and shows a negative trend. Fig. 6-10 also shows the correlation between total coherence ( $\gamma_{total}$ ) and field-estimated biomass.

### 6.3.3. PolInSAR Coherence Estimation for Height

Vegetation height was calculated using coherence amplitude. Fig. 6-11 compares the modeled height to the measured field height. The average height of each sample plot was used to validate the modeled height.

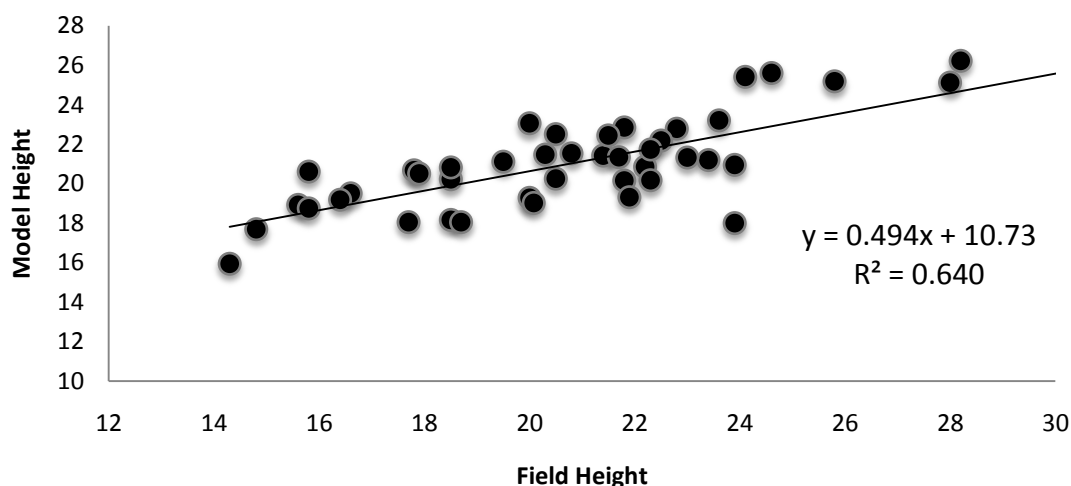


Figure 6-11: Modeled height vs. Field height.

The correlation between modeled and field height is 0.64, which shows that the modeled height compares reasonably with the field measured height. It has an RMSE of 6.2 m and a percent accuracy of 71.5%. The flat terrain of the Barkot Forest area has been a significant factor in accuracy of height estimation.

Fig. 6-12 presents the vegetation height estimated from coherence map. The red areas show lower heights ranging from 0 to 10m, green areas illustrate heights ranging from 10 to 20m and blue signifies heights from 20 to 30m. The red areas show river channels, roads and fields while the blue and green portions illustrate vegetation.

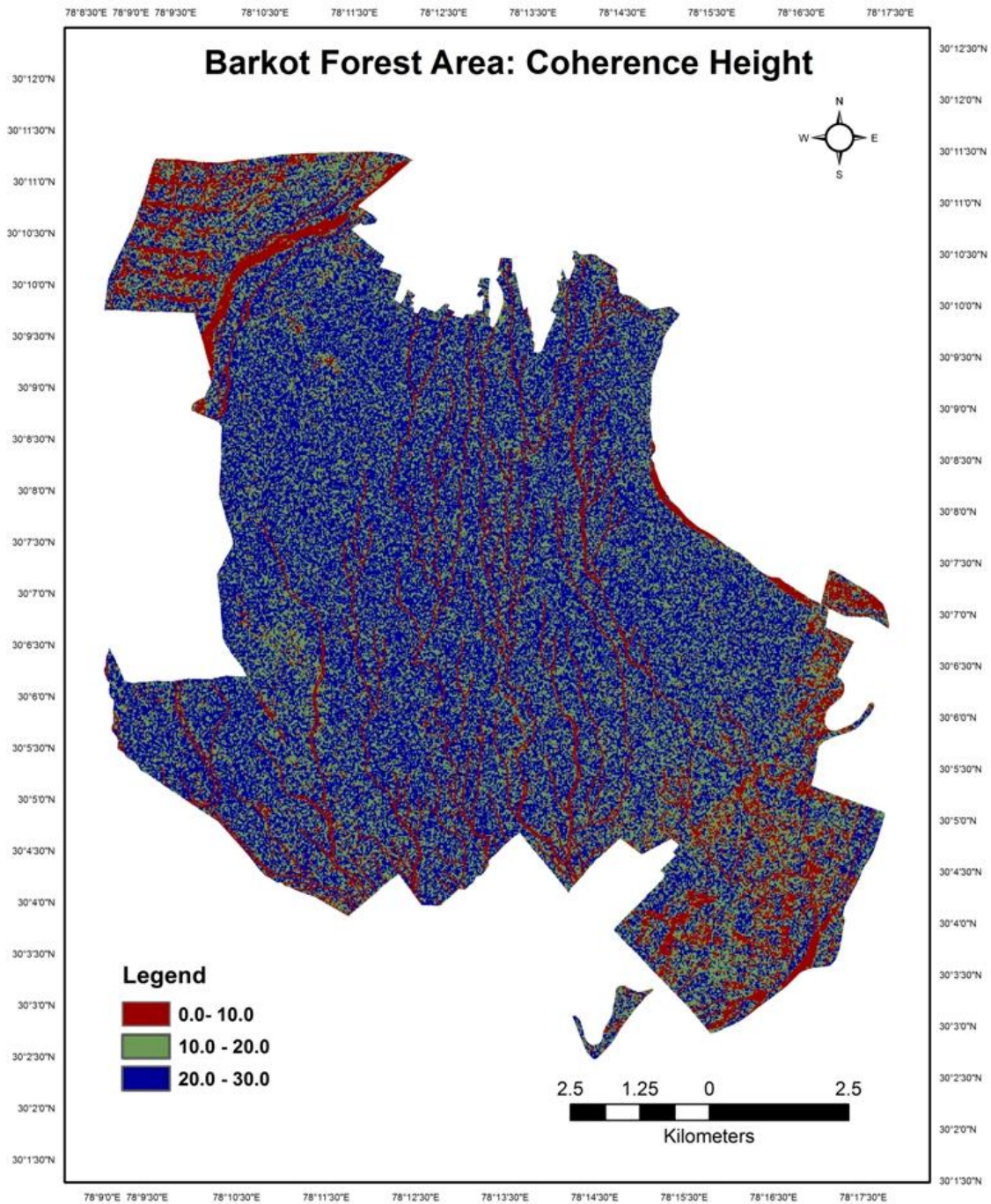


Figure 6-12: Coherence height in meters.

### 6.3.4. AGB Estimation from IWCM

The IWCM described in Chapter 5 was used to estimate AGB.

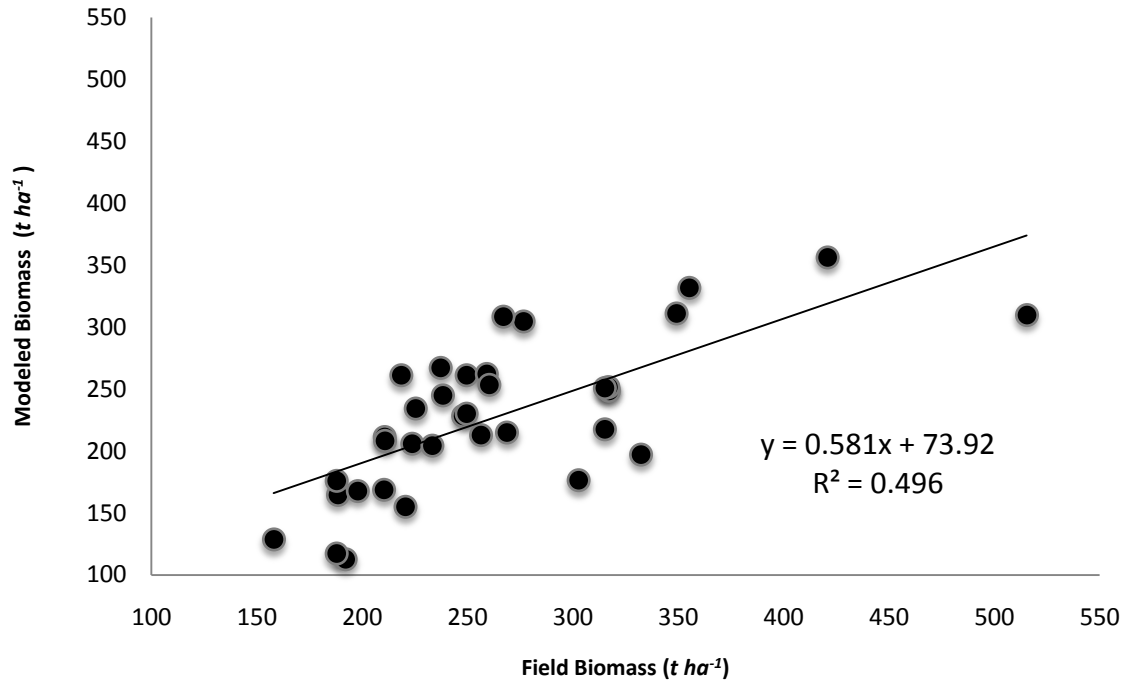


Figure 6-13: Field measured biomass vs. Modeled Biomass. The graph illustrates the correlation between the modeled biomass and the biomass calculated in the field.

Fig. 6-13 represents the similarity between the modeled AGB and the field estimated AGB with an  $R^2$  value of 0.5. The modeled AGB has an RMSE of  $62.73(t\ ha^{-1})$  and a percent accuracy of 51.



## 7. DISCUSSION

The main objective of this research was to estimate forest biophysical characteristics using PolInSAR techniques. AGB was modeled using decomposed backscatter as well as complex coherence and vegetation height was estimated using coherence amplitude. This chapter discusses the obtained results and highlights the strengths and weaknesses of the research work using S.W.O.T analysis.

### 7.1. Polarization Orientation Angle Shift

The effect of polarization orientation angle on PolSAR data was also observed and corrected for. The shift leads to an increase in the cross-pol intensity of the matrix, which results in an overestimation of volume scattering. Figures (6-3) and (6-6) illustrate that the values of volume scattering are overestimated when the orientation angle shift is not compensated for. This overestimation is induced by irregular terrain and performing de-orientation reduces the randomness in the orientation of the scatterers, thereby reducing the overall contribution of volume scattering to total backscatter in each plot.

Fig. 6-7 consists of two decomposed RGB images for the Master image. Image A is the one without deorientation while image B has been corrected for polarization orientation angle shift. The highlighted portions in the images show the difference in volume scattering before and after deorientation. Image 'A' shows the area as green, which illustrates volume scattering. The same area becomes red (red illustrates double bounce) after deorientation. The urban areas, which are not parallel to the satellite path, are classified as volume scatterers before deorientation. This change in colors signifies the overestimation of volume scattering and underestimation of double bounce scattering by polarization orientation angle shift and how deorientation enables its correction.

### 7.2. Backscatter vs. Biomass

Another relationship that can be derived from Figures (6-5) and (6-8) is that as biomass increases so do volume and total backscatter. The increasing trend of backscatter values with increasing biomass can also be seen in the JERS-1 data in the study by Santoro et al. [28]. The power of the volume scattering increases with an increase in biomass (Figures 6-2, 6-4), as volume power is directly dependent on biomass. Total backscatter is the sum of surface, volume and double bounce scattering, and an increase in the volume scattering will also result in an overall increase in total backscatter.

### 7.3. Coherence vs. Biomass

It is seen that as biomass increases, coherence decreases. The same trend can also be seen in the studies carried out by Wagner et al. [80] in a boreal forest in Siberia, Santoro [11] in

Northeast China and by Eriksson [81] in boreal forests in Russia.

Forests are natural mediums with lower coherence values as their orientation changes frequently and natural phenomena like rain, floods and etc. make forests an unstable scatterer. As biomass increases volume de-correlation also increases, thereby decreasing coherence.

#### **7.4. Vegetation Height**

The correlation between modeled and field measured vegetation height is 0.64, which shows that the modeled height compares reasonably with the field measured height. It has an RMSE of 6.2 m and a percent accuracy of 71.5%. The flat terrain of the Barkot Forest area has been a significant factor in accuracy of height estimation.

#### **7.5. AGB Estimation**

In studies carried out earlier [11],[74] IWCM modeling was done with single or dual polarimetric data. The limitation of single and dual polarimetric data is that it increases the number of unknown parameters that are used as input in the IWCM. These unknown parameters are then estimated using regression techniques, which lead to uncertainty in the retrieved parameters. With fully polarimetric data, most of the input parameters can be extracted from the data itself, reducing the ambiguity in IWCM. Using fully polarimetric data reduces the number of unknown parameters making the model less site dependent, making it applicable in the estimation of biophysical parameters for larger areas.

Previous studies have assessed AGB using SAR remote sensing in various forest types of the world. Mette [12] and Eriksson [81] achieved  $R^2$  values of 0.7 and 0.75 respectively, for their modeled AGB of boreal forests. The difference in the result obtained by them and the result of the current research work maybe due to the difference in the wavelengths of L-band and C-band. As L-band is a longer wavelength compared to C-band, its penetration capability may be a cause of the variation in the results.

In comparison to their results,  $R^2$  value of 0.5 and an RMSE of  $62.73(t\ ha^{-1})$  arrived at in the present study for tropical forests of Barkot Forest area, using data acquired by the C-band is comparatively accurate.

### 7.6. SWOT table

Table 7-1: SWOT table discussing the internal and external factors that either contribute to or limit the modeling approach of the current research work.

	<b>Strengths</b>	<b>Limitations</b>
<b>Internal Factors</b>	<p>Reduction of site dependence</p> <p>Less ambiguity in input model parameters</p> <p>Reasonable accuracy between modeled AGB and height and field measured AGB and height</p> <p>Estimation and corrections of Orientation angle shift on PolSAR data</p>	<p>Need more <i>in-situ</i> data</p> <p>Need to test given model in a more diverse study area</p> <p>Multi-frequency dataset for biomass estimation</p>
<b>External Factors</b>	<p>Penetration of cloud and canopy</p> <p>Speedy and large-scale estimation of biophysical parameters in comparison with traditional field methods</p> <p>Estimation of carbon present in tropical ecosystems</p>	<p>Uncertainty due to volumetric equations and specific gravity values that have been calculated by Forest Survey of India (FSI)</p> <p>Uncertainty due to GPS accuracy</p>

The main strength of using fully polarimetric data with PolInSAR lies in ensuring lesser ambiguity and site dependence, which helps in achieving comprehensive results for biophysical parameter retrieval, thereby reducing the expended time and energy. On the contrary, the uncertainties in volumetric equations and specific gravity data are limiting factors that need to be explored further. However, destructive sampling is prohibited in India and given the time for this research, the data from FSI was the only viable option. The limited accuracy of GPS readings was also observed as a limitation and this was addressed by taking readings in homogeneous areas.



## 8. CONCLUSION AND RECOMMENDATIONS

### 8.1. Conclusion

The main objective of this research was to estimate AGB using PolInSAR techniques in combination with semi-empirical modeling. In addition to AGB estimation, tree height has also been modeled using PolInSAR coherence estimation. Accordingly,  $R^2$  values of 0.5 for biomass and 0.64 for height were obtained for the Barkot Forest area in the present study. The RMSE and percent accuracy have also been assessed for these parameters. Modeled biomass values for the Barkot Forest area demonstrate a RMSE of  $62.73 (t ha^{-1})$  and a percent accuracy of 51%. The modeled height has shown a RMSE of 6.2 m and a percent accuracy of 71.5%, which compares favorably with the ground data.

It was seen that an increase in AGB values corresponded with an increase in the total backscatter values, especially in values of volume scattering. The effect of orientation angle shift was also studied and it was found that deorientation results in the correction of the overestimation of volume scattering caused by polarization orientation angle shift. It was also observed that an increase in biomass paralleled a decrease in total forest coherence. These backscatter and coherence values along with semi-empirically defined coefficient ( $\beta$ ) were the input parameters for the IWCM. Previous studies have estimated all of the input IWCM parameters using training data. However, in the present study the solitary unknown input parameter to the IWCM was  $\beta$ , which is related to forest transmissivity. The value of  $\beta$  has been calculated using a training set that encompasses the variations in biomass present in the forest stand.

The advantage of using fully polarimetric data in IWCM modeling lies in obviating the use of training sets in the estimation of the various input IWCM parameters, leading to significant reduction in site dependence. This methodology of extracting parameter values from fully polarimetric data also leads to reduced ambiguity of the outcome. The IWCM is already a robust model for biomass estimation, lesser site dependence and reduced ambiguity is likely to enhance the performance of this technique.

It has been recognized that tropical forests harbor 60% of the carbon present in the forests globally whereas they occupy just 40% of the global forest area. In comparison, the boreal and temperate forests occupy 60% of the global forest area while sequestering 40% of the carbon stored in forests [82]. Therefore, in redressal of the problem of increasing carbon emissions all over the world, tropical forests warrant greater conservation attention. It emerges that studies based on the use of fully polarimetric data with PolInSAR coherence estimation can serve as a ready tool for assessing biomass.

## 8.2. Recommendations

A few recommendations have been listed for future studies to enhance the reliability of modeling approach for AGB estimation.

- The current project observes and compensates for the effect of polarization orientation angle shift on total forest backscatter. It is recommended that a similar approach maybe adopted for total forest coherence in further research.
- The present study used fully polarimetric, C-band data in the PolInSAR coherence estimation for estimating biomass for a tropical forest area. A multi-frequency approach using a wider spectrum of microwave bands would enhance the accuracy of biomass estimation. The proposed model's efficiency should further be tested with other datasets and sites. The Barkot Forest area comprises of a mature Sal forest, thereby providing a homogenous environment. It is suggested that various forest types comprising of different stages of succession with a heterogeneous mix of species should also be studied using the present methodology. This should help in the assessment of all forest types prevalent within the tropical landscape.
- Inclusion of additional parameters like the effect of soil, leaf and stem moisture may further enhance the interpretation and accuracy of biomass estimation.

## REFERENCES

- [1] R. Costanza, R. d' Arge, R. de Groot, S. Farber, M. Grasso, B. Hannon, K. Limburg, S. Naeem, R. V. O'Neill, J. Paruelo, R. G. Raskin, P. Sutton, and M. van den Belt, "The value of the world's ecosystem services and natural capital," *Nature*, vol. 387, no. 6630, pp. 253–260, 1997.
- [2] "UNDP Annual Report 2008." 26-Aug-2013. [Online]. Available: [http://www.undp.org/content/undp/en/home/librarypage/corporate/undp\\_in\\_action\\_2008/](http://www.undp.org/content/undp/en/home/librarypage/corporate/undp_in_action_2008/).
- [3] I. H. Woodhouse, *Introduction to microwave remote sensing*. Boca Raton: Taylor & Francis, 2006, pp. 262-264
- [4] S. Cloude, *Polarisation: Applications in Remote Sensing*. Oxford University Press, 2009, pp.71-270.
- [5] T. Mette, K. Papathanassiou, and I. Hajnsek, "Biomass estimation from polarimetric SAR interferometry over heterogeneous forest terrain," in *Geoscience and Remote Sensing Symposium, 2004 IGARSS'04*. vol. 1, pp. 511–514, 20<sup>th</sup>-24<sup>th</sup> Sept. 2004.
- [6] "State of the world's forests. Rome: Food and Agriculture Organization of the United Nations", 5-Sept-2013. [Online] <http://www.fao.org/docrep/003/y0900e/y0900e00.htm>, 2001.
- [7] M. L. Imhoff, "Radar backscatter and biomass saturation: ramifications for global biomass inventory," *IEEE Transactions on Geoscience and Remote Sensing*, vol. 33, no. 2, pp. 511–518, 1995.
- [8] L. V. Bertalanffy, *Theoretische Biologie, Band II: Stoffwechsel, Wachstum*. Francke AG Verlag, 1951.
- [9] M. Neumann, "Remote sensing of vegetation using multi-baseline polarimetric SAR interferometry: theoretical modeling and physical parameter retrieval," Ph. D Thesis, Université de Rennes 1, France, 2009.
- [10] S. R. Cloude and K. P. Papathanassiou, "Coherence optimisation in polarimetric SAR interferometry," *Geoscience and Remote Sensing, IGRASS'97*, vol. 4, pp. 1932–1934, 3-8 Aug, 1997.
- [11] M. Santoro, "Estimation of biophysical parameters in boreal forests from ERS and JERS SAR interferometry," Ph. D Thesis. Department of Radio and Space Science, Chalmers University of Technology, 2003.
- [12] T. Mette, "Forest Biomass Estimation from Polarimetric SAR Interferometry," Ph.D Thesis, Faculty and Weihenstephan Science Center Nutrition, land use and environment, Technical University of Munich, 2007.
- [13] A. Freeman and S. L. Durden, "A three-component scattering model for polarimetric SAR data," *IEEE Transactions on Geoscience and Remote Sensing*, vol. 36, no. 3, pp. 963–973, 1998.
- [14] R. N. Treuhaft, S. N. Madsen, M. Moghaddam, and J. J. van Zyl, "Vegetation characteristics and underlying topography from interferometric radar," *Radio Science*, vol. 31, no. 6, pp. 1449–1485, 1996.
- [15] R. N. Treuhaft and P. R. Siqueira, "Vertical structure of vegetated land surfaces from interferometric and polarimetric radar," *Radio Science*, vol. 35, no. 1, pp. 141–177, 2000.
- [16] D. Lu, "The potential and challenge of remote sensing- based biomass estimation," *International Journal of Remote Sensing*, vol. 27, no. 7, pp. 1297–1328, 2006.
- [17] S. Kumar, "Retrieval of forest parameters from Envisat ASAR data for biomass inventory in dudhwa national park, U.P., India," MSc Thesis, ITC, International Institute for geo-information science and earth observation, 2009.
- [18] Forest Resource Assessment. Rome: Food and Agriculture Organization of the United Nations, 6-Sept-2013. [Online] <http://www.fao.org/docrep/013/i1757e/i1757e.pdf>, 2001.
- [19] N. S. Goel, "Models of vegetation canopy reflectance and their use in estimation of biophysical parameters from reflectance data," *Remote Sensing Reviews*, vol. 4, no. 1, pp. 1–212, 1988.
- [20] A. N. Arslan, J. Koskinen, J. Pulliainen, and M. Hallikainen, "A semi empirical backscattering model of forest canopy covered by snow using SAR data," presented at the *Geoscience and Remote Sensing Symposium, 2000 IGARSS 2000*, vol.5, pp.1904-1906, 24<sup>th</sup> -28<sup>th</sup> July, 2000.
- [21] M. D. Behera, S. P. S. Kushwaha, and P. S. Roy, "Forest Vegetation Characterization and Mapping Using IRS-1C Satellite Images in Eastern Himalayan Region," *Geocarto International*, vol. 16, no. 3, pp. 53–62, 2001.
- [22] J. Dong, R. K. Kaufmann, R. B. Myneni, C. J. Tucker, P. E. Kauppi, J. Liski, W. Buermann, V. Alexeyev, and M. K. Hughes, "Remote sensing estimates of boreal and temperate forest woody

- biomass: carbon pools, sources, and sinks,” *Remote Sensing of Environment*, vol. 84, no. 3, pp. 393–410, 2003.
- [23] F.M. Henderson and A.J. Lewis, *Principles and Applications of Imaging Radar; Manual of Remote Sensing*, American Society for Photogrammetry and Remote Sensing, vol. 2., 3rd. ed. New York: J. Wiley, 1998, pp. 1-811.
- [24] E. Luneburg, “Aspects of radar polarimetry,” *Turkish Journal of Electrical Engineering*, vol. 10, no. 2, 2002.
- [25] J. C. Curlander, *Synthetic aperture radar: systems and signal processing*. New York: Wiley, 1991, pp.1-672.
- [26] D. Massonnet and J.C. Souyris, *Imaging with synthetic aperture radar*. Lausanne, Switzerland: EPFL Press, 2008, pp. 26-39.
- [27] J. Carreiras, J. Melo, and M. Vasconcelos, “Estimating the Above-Ground Biomass in Miombo Savanna Woodlands (Mozambique, East Africa) Using L-Band Synthetic Aperture Radar Data,” *Remote Sensing of Environment*, vol. 5, no. 4, pp. 1524–1548, 2013.
- [28] M. Santoro, L. Eriksson, J. Askne, and C. Schmullius, “Assessment of stand-wise stem volume retrieval in boreal forest from JERS-1 L-band SAR backscatter,” *International Journal of Remote Sensing*, vol. 27, no. 16, pp. 3425–3454, 2006.
- [29] R. Bindlish and A. P. Barros, “Parameterization of vegetation backscatter in radar-based, soil moisture estimation,” *Remote Sensing of Environment*, vol. 76, no. 1, pp. 130–137, 2001.
- [30] S. Cloude, *Polarisation: applications in remote sensing*, 1st ed. Oxford; New York: Oxford University Press, 2010. pp.71-270
- [31] R. Touzi, W. M. Boerner, J. S. Lee, and E. Lueneburg, “A review of polarimetry in the context of synthetic aperture radar: concepts and information extraction,” *Canadian Journal of Remote Sensing*, vol. 30, no. 3, pp. 380–407, 2004.
- [32] H. Skriver, “Signatures of polarimetric parameters and their implications on land cover classification,” presented at the *Geoscience and Remote Sensing Symposium, 2007 IGARSS 2007*, pp.4195-4198, 23rd -28th July, 2007.
- [33] G. Sinclair, "Modification of the radar target equation for arbitrary targets and arbitrary polarization", Technical Report pp.302–19, The Ohio State University Research Foundation, Antenna Laboratory, 1948.
- [34] G. Sinclair, “The Transmission and Reception of Elliptically Polarized Waves,” *Proceedings of the IRE*, vol. 38, no. 2, pp. 148–151, 1950.
- [35] E. M.Kennaugh, “Effects of the Type of Polarization on Echo Characteristics,” Reports 381-1 to 394-24, Antenna Laboratory, The Ohio State University Research Foundation, 1949-1954.
- [36] E. M. Kennaugh, “Polarization Properties of Radar Reflections,” Master's Thesis, Ohio State University, Columbus, 1952.
- [37] J. R. Huynen., “Phenomenological Theory of Radar Targets,” Ph.D Thesis, University of Technology, Delft, The Netherlands, 1970.
- [38] S. R. Cloude and E. Pottier, “An entropy based classification scheme for land applications of polarimetric SAR,” *IEEE Transactions on Geoscience and Remote Sensing*, vol. 35, no. 1, pp. 68–78, 1997.
- [39] W. M. Boerner, “Basic Concepts In Radar Polarimetry,” UIC-ECE Communications, Sensing & Navigation Laboratory, Chicago, USA, Lecture Notes, 1998, pp. 30-32.
- [40] C. Putignano, “PolSOM and TexSOM in Polarimetric SAR Classification,” Ph.D Thesis, Tor Vergata University, Rome, Italy, 2009.
- [41] J. S. Lee and E. Pottier, *Polarimetric radar imaging: from basics to applications*. Boca Raton: CRC Press, 2009. pp. 1-10.
- [42] J. S. Lee, T. L. Ainsworth, D. L. Schuler, D. Kasilingam, and W. M. Boerner, “Interpreting off-diagonal terms in polarimetric coherency matrix,” *Geoscience and Remote Sensing Symposium, 2001. IGARSS '01*, vol. 2, pp. 913–915, 9th-13th July, 2001.
- [43] Xinyi Shen, Yang Hong, Qiming Qin, Weilin Yuan, Sheng Chen, Shaohua Zhao, and T. Grout, “Orientation Angle Calibration for Bare Soil Moisture Estimation Using Fully Polarimetric SAR Data,” *IEEE Transactions on Geoscience and Remote Sensing*, vol. 49, no. 12, pp. 4987–4996, 2011.
- [44] J. S. Lee, D. L. Schuler, T. L. Ainsworth, and W. M. Boerner, “Polarization orientation estimation and applications: a review,” *Geoscience and Remote Sensing Symposium, 2003. IGARSS '03*, vol. 1, pp. 428–430, 21st -25th Jul, 2003.

- [45] J. S. Lee, D. L. Schuler, and T. L. Ainsworth, "Polarimetric SAR data compensation for terrain azimuth slope variation," *IEEE Transactions on Geoscience and Remote Sensing*, vol. 38, no. 5, pp. 2153–2163, 2000.
- [46] F. Xu and J. Ya-Qiu, "Deorientation theory of polarimetric scattering targets and application to terrain surface classification," *IEEE Transactions on Geoscience and Remote Sensing*, vol. 43, no. 10, pp. 2351–2364, 2005.
- [47] J. S. Lee and T. L. Ainsworth, "The Effect of Orientation Angle Compensation on Coherency Matrix and Polarimetric Target Decompositions," presented at 8th European Conference on the Synthetic Aperture Radar (EUSAR), pp. 1–4, 7<sup>th</sup> -10<sup>th</sup> Jun, 2010.
- [48] "Single Multi Polarization SAR data," 18-Sep-2013. [Online]. Available: [www.envisat.esa.int](http://www.envisat.esa.int).
- [49] Y. Yamaguchi, T. Moriyama, M. Ishido, and H. Yamada, "Four-component scattering model for polarimetric SAR image decomposition," *IEEE Transactions on Geoscience and Remote Sensing*, vol. 43, no. 8, pp. 1699–1706, 2005.
- [50] T. Moriyama, "Polarimetric SAR Image Analysis Using Model Fit for Urban Structures," *IEICE Transactions on Communications*, vol. E88-B, no. 3, pp. 1234–1243, 2005.
- [51] Lamei Zhang, Bin Zou, Hongjun Cai, and Ye Zhang, "Multiple-Component Scattering Model for Polarimetric SAR Image Decomposition," *IEEE Geoscience and Remote Sensing Letters*, vol. 5, no. 4, pp. 603–607, 2008.
- [52] H. A. Zebker and R. M. Goldstein, "Topographic mapping from interferometric synthetic aperture radar observations," *Journal of Geophysical Research*, vol. 91, no. B5, p. 4993, 1986.
- [53] E. R. Caro, R. M. Goldstein, and C. Wu, "Method and Apparatus for Contour Mapping Using Synthetic Aperture Radar," Government Patent, NASA, 1983.
- [54] F. K. Li and R. M. Goldstein, "Studies of multibaseline spaceborne interferometric synthetic aperture radars," *IEEE Transactions on Geoscience and Remote Sensing*, vol. 28, no. 1, pp. 88–97, 1990.
- [55] U. Wegmuller and C. L. Werner, "SAR interferometric signatures of forest," *IEEE Transactions on Geoscience and Remote Sensing*, vol. 33, no. 5, pp. 1153–1161, 1995.
- [56] U. Wegmuller and C. Werner, "Retrieval of vegetation parameters with SAR interferometry," *IEEE Transactions on Geoscience and Remote Sensing*, vol. 35, no. 1, pp. 18–24, 1997.
- [57] M. Santoro, J. Askne, and P. B. Dammert, "Tree height estimation from multi-temporal ers sar interferometric phase," *Fringe Proceedings, ESA-ESRIN*, 1<sup>st</sup>-5<sup>th</sup> Dec, 2003.
- [58] K. P. Papathanassiou and S. R. Cloude, "Single-baseline polarimetric SAR interferometry," *IEEE Transactions on Geoscience and Remote Sensing*, vol. 39, no. 11, pp. 2352–2363, 2001.
- [59] S. R. Cloude and K. P. Papathanassiou, "Three-stage inversion process for polarimetric SAR interferometry," *IEEE Proceedings on Radar, Sonar and Navigation*, vol. 150, no. 3, pp. 125-134, 2003.
- [60] S. R. Cloude and K. P. Papathanassiou, "Polarimetric SAR interferometry," *IEEE Transactions on Geoscience and Remote Sensing*, vol. 36, no. 5, pp. 1551–1565, 1998.
- [61] T. Aulinger, T. Mette, K. P. Papathanassiou, I. Hajnsek, M. Heurich, and P. Krzystek, "Validation of Heights from Interferometric SAR and LIDAR over the Temperate Forest Site 'Nationalpark Bayerischer Wald,'" in *ESA Special Publication*, vol. 586, pp. 11, 2005.
- [62] L. Sagues, J. M. Lopez-Sanchez, J. Fortuny, X. Fabregas, A. Broquetas, and A. J. Sieber, "Indoor experiments on polarimetric SAR interferometry," *IEEE Transactions on Geoscience and Remote Sensing*, vol. 38, no. 2, pp. 671–684, 2000.
- [63] J. D. Ballester-Berman, J. M. Lopez-Sanchez, and J. Fortuny-Guasch, "Retrieval of biophysical parameters of agricultural crops using polarimetric SAR interferometry," *IEEE Transactions on Geoscience and Remote Sensing*, vol. 43, no. 4, pp. 683–694, 2005.
- [64] R. Z. Schneider, K. Papathanassiou, I. Hajnsek, and A. Moreira, "Polarimetric interferometry over urban areas: information extraction using coherent scatterers," *Geoscience and Remote Sensing Symposium, 2005. IGARSS '05*, vol. 2, pp. 913–915, , vol. 2, pp. 1089–1092, 25<sup>th</sup> -29<sup>th</sup> Jun ,2005.
- [65] F. Garestier, P. Dubois-Fernandez, X. Dupuis, P. Paillou, and I. Hajnsek, "PolInSAR analysis of X-band data over vegetated and urban areas," *IEEE Transactions on Geoscience and Remote Sensing*, vol. 44, no. 2, pp. 356–364, 2006.
- [66] L. Ferro-Famil, F. Kugler, E. Pottier, and J. S. Lee, "Forest mapping and classification at L band using POL-inSAR optimal coherence set statistics," *EUSAR*, 16<sup>th</sup>-18<sup>th</sup> May, 2006.

- [67] M. Neumann, L. Ferro-Famil, and A. Reigber, "Estimation of Forest Structure, Ground, and Canopy Layer Characteristics From Multibaseline Polarimetric Interferometric SAR Data," *IEEE Transactions on Geoscience and Remote Sensing*, vol. 48, no. 3, pp. 1086–1104, 2010.
- [68] M. Lavalle, "Full and compact polarimetric radar interferometry for vegetation remote sensing," Ph.D Thesis, Université Rennes 1, 2009.
- [69] H. A. Zebker and J. Villasenor, "Decorrelation in interferometric radar echoes," *IEEE Transactions on Geoscience and Remote Sensing*, vol. 30, no. 5, pp. 950–959, 1992.
- [70] D. Mahanta, R. Bhattacharyya, K. A. Gopinath, M. D. Tuti, C. L. Mina, B. M. Pandey, P. K. Mishra, J. K. Bisht, A. K. Srivastva, and J. C. Bhatt, "Influence of farmyard manure application and mineral fertilization on yield sustainability, carbon sequestration potential and soil property of gardenpea–french bean cropping system in the Indian Himalayas," *Scientia Horticulturae*, vol. 164, pp. 414–427, Dec. 2013.
- [71] H. G. Champion and S. K. Seth, *A revised survey of the forest types of India*. Government of India press, New Delhi, India, 1968, pp. 343-388.
- [72] Forest Survey of India, *Volume Equations for Forests of India, Nepal and Bhutan*, Ministry of Environment and Forests, Dehra Dun, India., 1996, pp. 1-249.
- [73] V.D. Limaye and B.R. Sen, "*Weight and Specific Gravity of Indian Woods*," Forest Research Institute, Indian Forest Records, vol. I–VI, Dehradun, India, 1956.
- [74] J. Askne, P. B. G. Dammert, P. Fransson, H. Israelsson, and L. M. H. Ulander, "Retrieval of forest parameters using intensity and repeat-pass interferometric SAR information," *Proceedings of Retrieval of Bio- and Geophysical Parameters from SAR Data for Land Applications*, Toulouse, pp. 119–129, 1995.
- [75] J. Praks, F. Kugler, K. P. Papathanassiou, I. Hajnsek, and M. Hallikainen, "Height Estimation of Boreal Forest: Interferometric Model-Based Inversion at L- and X-Band Versus HUTSCAT Profiling Scatterometer," *IEEE Geoscience and Remote Sensing Letters*, vol. 4, no. 3, pp. 466–470, 2007.
- [76] H. J. C. van Leeuwen, "Multifrequency And Multitemporal Analysis Of Scatterometer Radar Data With Respect To Agricultural Crops Using The Cloud Model." *Geoscience and Remote Sensing Symposium, 1991. IGARSS '91*, vol. 4, pp. 1893–1897, 3<sup>rd</sup> -6<sup>th</sup>, Jun, 1991.
- [77] J. T. Pulliainen, K. Heiska, J. Hyypä, and M. T. Hallikainen, "Backscattering properties of boreal forests at the C- and X-bands," *IEEE Transactions on Geoscience and Remote Sensing*, vol. 32, no. 5, pp. 1041–1050, 1994.
- [78] S. Kumar, U. Pandey, S. P. Kushwaha, R. S. Chatterjee, and W. Bijker, "Aboveground biomass estimation of tropical forest from Envisat advanced synthetic aperture radar data using modeling approach," *Journal of Applied Remote Sensing*, vol. 6, no. 1, pp. 063588, 2012.
- [79] H. Wang and K. Ouchi, "A Simple Moment Method of Forest Biomass Estimation From Non-Gaussian Texture Information by High-Resolution Polarimetric SAR," *IEEE Geoscience and Remote Sensing Letters*, vol. 7, no. 4, pp. 811–815, 2010.
- [80] W. Wagner, J. Vietmeier, C. Schmullius, M. Davidson, T. L. Toan, S. Quegan, J. Yu, A. Luckman, K. Tansey, H. Balzter, and D. Gaveau, "The use of coherence information from ERS tandem pairs for determining forest stock volume in SIBERIA," *Geoscience and Remote Sensing Symposium, 2000. IGARSS '00*, vol. 4, pp. 1396–1398, 24<sup>th</sup>-28<sup>th</sup> Jul, 2000.
- [81] L. E. B. Eriksson, "Satellite-borne L-band Interferometric Coherence for Forestry Applications is the Boreal Zone," Ph. D Thesis, Friedrich-Schiller-University Jena, Germany, 2004.
- [82] R. K. Dixon, S. Brown, R. A. Houghton, A. M. Solomon, M. C. Trexler, and J. Wisniewski, "Carbon Pools Flux of Global Forest Ecosystems," *Science*, vol. 263, no.5144, pp. 185–190, 1994.

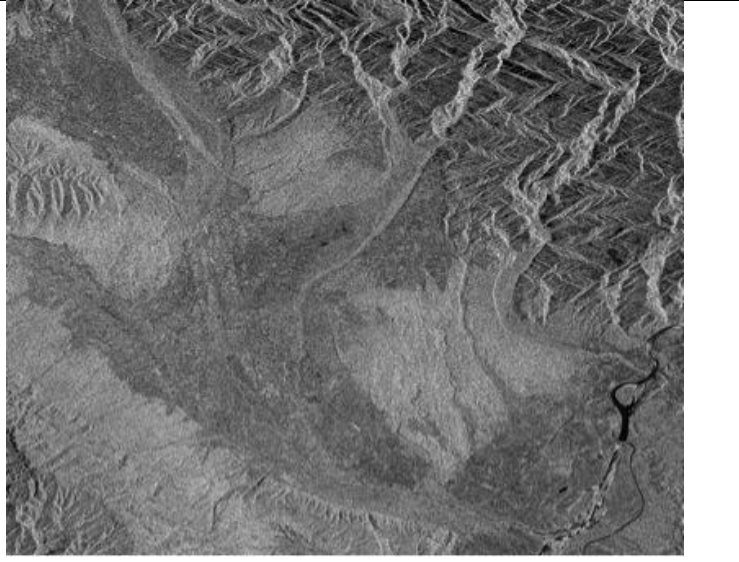
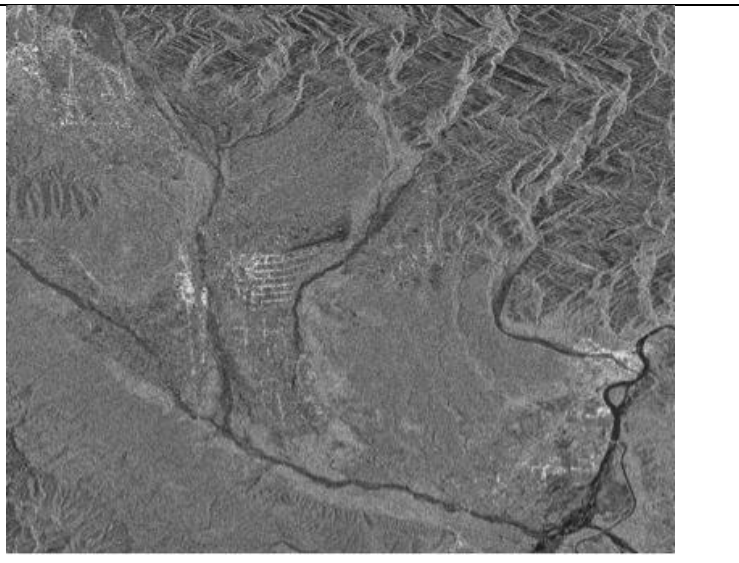
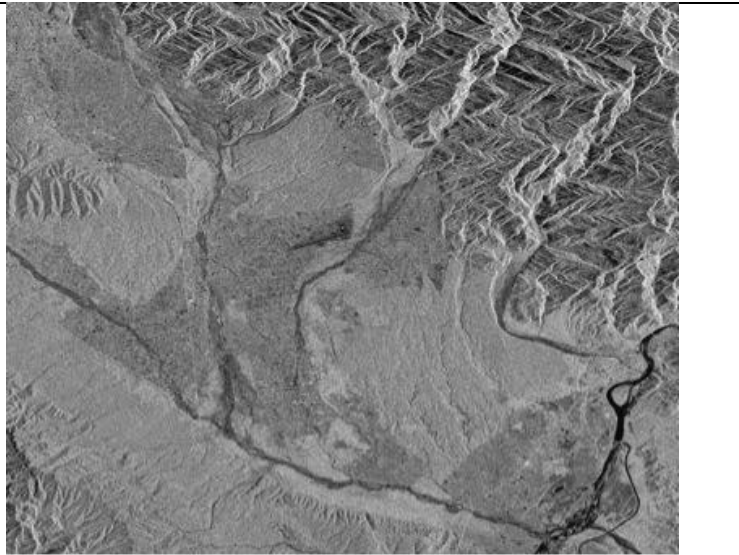
**APPENDIX 1: VOLUMETRIC EQUATIONS: FSI**

S.No	Species	Botanical Name	Volumetric Equations
1	Amaltash	Cassia fistula L.	$0.066+0.287 \times D_2 \times H$
2	Awla	Phyllanthus emblica L.	$0.13734-2.49039 \times D+15.59566 \times D_2-11.06205 \times D_3$
3	Bakli	Anogeissus latifolia Roxb. ex DC.	$(0.46976+5.99849 \times D-2.60729) \times 2$
4	Bel	Aegle marmelos (L.) Correa	$0.000342+0.0922 \times D+2.28178 \times D_2 \times H$
5	Chamror	Ehretia laevis Roxb.	$(-0.03844+0.94649 \times D-5.40987 \times D_2+33.17338 \times D_3)$
6	Domsal	Miliusa velutina (Dunal) Hook. f. & Th.	$0.00855+0.4432 \times D_2+0.28813 \times D_2 \times H$
7	Haldu	Adina cordifolia (Roxb.) Hook. f.	$(-0.16354+2.81144 \times D) \times 2$
8	Jamun	Syzgium cumini (L.) Skeels	$0.09809-1.94468 \times D+13.36728 \times D_2-6.33263 \times D_3$
9	Kanju	Holoptelea integriflora (Roxb.) Planch.	$0.00342-0.0922 \times D+2.28178 \times D_2+9.46641 \times D_3$
10	Khair	Acacia catechu (L.f.) Willd.	$0.02384-0.72161 \times D+7.46888 \times D_2$
11	Lanthus	Ailanthus excels Roxb.	$(0.32056+5.16781 \times D-1.83345) \times 2$
12	Lissora	Cordia oblicua Willd.	$(-0.49388+7.56417 \times D-31.45373 \times D_2+50.93877 \times D_3)$
13	Lyptis	Eucalyptus species	$0.02894-0.89284 \times D+8.72416 \times D_2$
14	Rohini	Mallotus philippensis (Lamk) Muell.-Arg.	$0.14749-2.87503 \times D+19.61977 \times D_2-19.1163 \times D_3$
15	Sal	Shorea robusta Gaertn f.	$(0.16306+4.8991 \times D-1.57402 \times D) \times 2$
16	Sehen	Terminalia alata Heyne ex Roth	$0.08658-2.04096 \times D+13.28405 \times D_2-3.58047 \times D_3$
17	Semal	Bombax ceiba L.	$(-0.032-0.619 \times D+7.208 \times D_2)$
18	Shisham	Dalbergia sissoo Roxb.	$(-0.013703+3.943499 \times D_2)$
19	Teak	Tectona grandis L. f.	$0.08847-1.46936 \times D+11.98979 \times D_2+1.97056 \times D_3$
20	Tun	Toona ciliata Roem.	$1.10314-3.52579+15.50182 \times D_2$

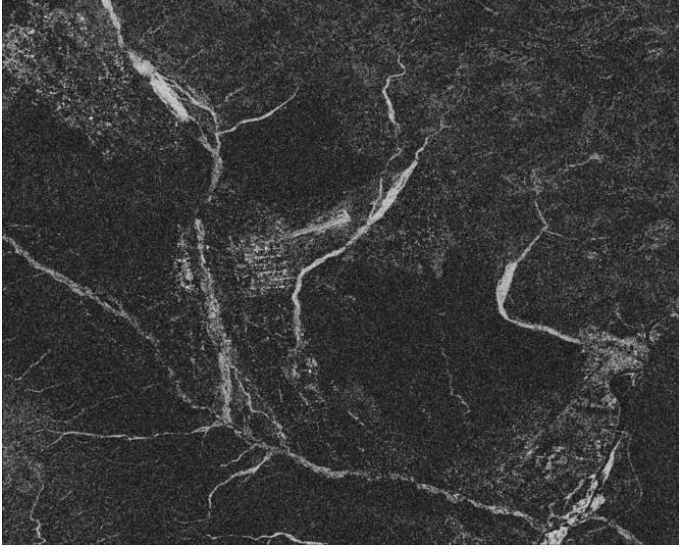
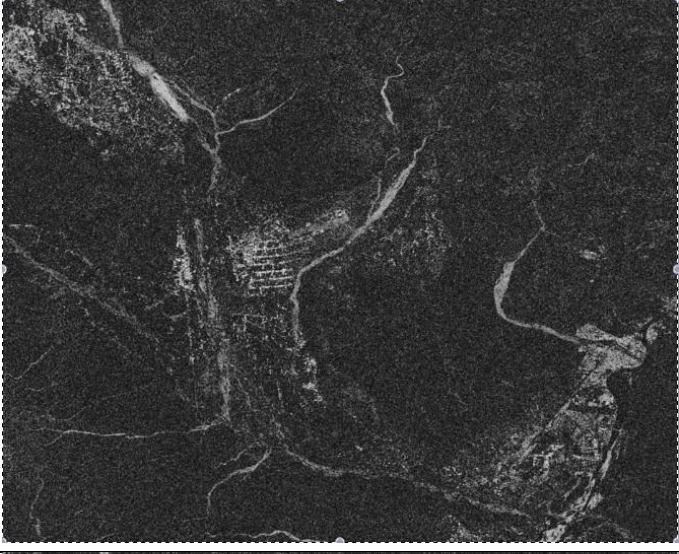
## Appendix 2: Specific Gravity Values

Local Name	Botanical Name	Specific Gravity
Amaltas	<i>Cassia fistula</i> L.	0.746
Awla	<i>Phyllanthus emblica</i> L.	0.75
Bakli	<i>Anogeissus latifolia</i> Roxb. ex DC.	0.62
Bel	<i>Aegle marmelos</i> (L.) Correa	0.754
Chamror	<i>Ehretia laevis</i> Roxb.	0.571
Domsal	<i>Milium velutinum</i> (Dunal) Hook. f. & Th.	0.615
Haldu	<i>Adina cordifolia</i> (Roxb.) Hook. f.	0.68
Jamun	<i>Syzgium cumini</i> (L.) Skeels	0.647
Kanju	<i>Holoptelea integriflora</i> (Roxb.) Planch.	0.498
Khair	<i>Acacia catechu</i> (L.f.) Willd.	0.88
Lanthus	<i>Ailanthus excelsa</i> Roxb.	0.5
Lissora	<i>Cordia obliqua</i> Willd.	0.73
Lyptis	<i>Eucalyptus</i> species	0.79
Rohini	<i>Mallotus philippensis</i> (Lamk) Muell.-Arg.	0.571
Sal	<i>Shorea robusta</i> Gaertn f.	0.728
Sehen	<i>Terminalia alata</i> Heyne ex Roth	0.63
Semal	<i>Bombax ceiba</i> L.	0.8
Shisham	<i>Dalbergia sissoo</i> Roxb.	0.69
Teak	<i>Tectona grandis</i> L. f.	0.57
Tun	<i>Toona ciliata</i> Roem.	0.625

**Appendix 3: Polarimetric decomposition of Radarsat -2 data for Barkot Forest Range (Master image)**

<b>Surface scattering</b>	
<b>Double Bounce Scattering</b>	
<b>Volume Scattering</b>	

### Appendix 4: Complex Coherence Estimation

<p><b>Coherence from Surface scattering (HH-VV)</b></p>	
<p><b>Coherence from Double bounce scattering (HH+VV)</b></p>	
<p><b>Coherence from Volume scattering (HV+VH)</b></p>	